ABSTRACT

MISHRA, ANAND VARDHAN. Development of Boundary Conditions for Turbulent Flow in a Channel with Nucleating Bubbles. (Under the direction of Dr. Igor A. Bolotnov).

Effect of nucleating bubbles on turbulent flow in a channel is quantified through DNS simulations for different nucleating bubble densities. Single phase Navier-Stokes equations are solved using finite element method and bubbles are represented as rigid stationary hemispherical obstacles at the wall with zero-velocity condition. Six different cases were analyzed including channel with smooth wall and channel with rough wall with five different bubble nucleation densities. Friction factor and the turbulence law of the wall were obtained for each case. They were further related with the previously published results for correlation of nucleating bubble density with heat flux to arrive at a correlation between heat flux and friction factor and the law of the wall constants. This leads to insight in how the nucleating bubbles modify the turbulence in boiling flows. To quantify the effect of deformable nucleating bubbles dynamic and static contact angle has been implemented in PHASTA and shown for a single bubble.

Development of Boundary Conditions for Turbulent Flow in a Channel with Nucleating Bubbles

by
Anand Vardhan Mishra

A thesis submitted to the Graduate Faculty of
North Carolina State University
in partial fulfillment of the
requirements for the degree of
Master of Science

Nuclear Engineering

Raleigh, North Carolina

2013

APPROVED BY:

_____	_____
Dr. I. A. Bolotnov Committee Chair	Dr. N. Dinh

_____
Dr. J. Edwards

DEDICATION

"There is no wealth but life"- John Ruskin

To my parents, my brother and to the cities of Tokyo and Vienna.

BIOGRAPHY

The author graduated from Indian Institute of Technology (IIT) Kanpur with the degree of Bachelor of Technology in Mechanical Engineering in 2011. As a student at IIT Kanpur he worked to generate interest among the student community about energy efficiency and generation and co-founded the Group for Environment & Energy Engineering (GE3). During his undergraduate career he was awarded the Young Engineer and Scientist Award in 2010 by the Honda Foundation Japan following which he did his summer internship in 2010 at the Nuclear Engineering Department of Tokyo Institute of Technology. During his stay at Tokyo he decided to study further. He joined the Department of Nuclear Engineering at North Carolina State University in 2011 for his graduate studies under the supervision of Dr. Igor A. Bolotnov. In his free time the author pursues his hobbies of travelling, backpacking and fitness training.

ACKNOWLEDGMENTS

I would like to thank Dr. Igor A. Bolotnov without whom I would not have been able to complete this thesis. I express my deepest gratitude to my teachers Prof. Prabhat Munshi and Prof. Hisahi Ninokata who initiated me into the field of nuclear engineering. I would also like to thank Mr. V.K. Bansal who gave me the formulae for life and Mr. R.K. Verma who helped me through the toughest time of my life yet. I would like to thank my mathematics teachers Mr. Prakash Dwivedi and the late Mr. S. S. Dave, they removed the fear of mathematics from within me. I am what my teachers have made me and I hope I always have their blessings in life. I would like to thank Papa for never allowing me to settle for anything less than the absolute best I could get. I want to thank my mummy who guided me and made me understand the key to happiness. I want to thank my brother Aditya who probably does not even realize how far he went beyond his abilities to support me when I needed it the most. I want to thank my Mama and Mami, Nana and Nani, Dada and Dadi to help me become the person I am.

I want to thank my friends who helped me and have shared with me whatever memories I have of past six and half years of college life in India and in the U.S.A. All B-Top guys and especially my band of brothers, Rahul Singh, Enthu, ParasP, AK Rai and Sumit. Thanks to Kali and Dude because they helped me to formulate my ideas in a way no other did. I also want to thank my friends here especially Rudro, Nathan, Devon, Christine, Bassam, Pietro, Eric and Stoeffel helping me when I really needed it and making my life so much more fun! I will remember them long after! A big thanks to all the Gentlemen's Batch of Mechanical Engineering 2007 at IIT Kanpur, especially Chidiya, Paras, Jais, Manna,

DOAA, Verma-ji, Dhama, Apoorva, Bhatera, Boxer, Chaddha, Pankaj, Ayush, Prakhar and all others who will be mad because I did not write their names. I am also grateful to the staff at N.C. State especially Hermine who made my life a little easy here in Raleigh.

TABLE OF CONTENTS

LIST OF TABLES

LIST OF FIGURES

1. INTRODUCTION

Direct numerical simulation (DNS) has become an important tool to help develop new models for computational multiphase fluid dynamics (CMFD) [1]. The detailed understanding of boiling process in turbulent flow is one of the most interesting challenge problems that are faced today. To specifically quantify flow parameters and the effect of bubbles at different stages of boiling a system of separate effect studies have been conducted by Bolotnov et.al.[2, 3]. Analysis of two-phase bubbly flow to quantify the effect of bubbles on turbulence has been performed by Bolotnov (Fig. 1). In the present study the bubbles have been modeled as rigid fixed hemispherical objects on the wall to quantify the effect of nucleating bubbles during the boiling process. The distribution of hemispherical roughness elements on a wall to predict the influence of nucleating bubbles on fuel rods in reactor conditions was suggested earlier by Chatzikyriakou et.al.[4]. This study puts that idea into practice.

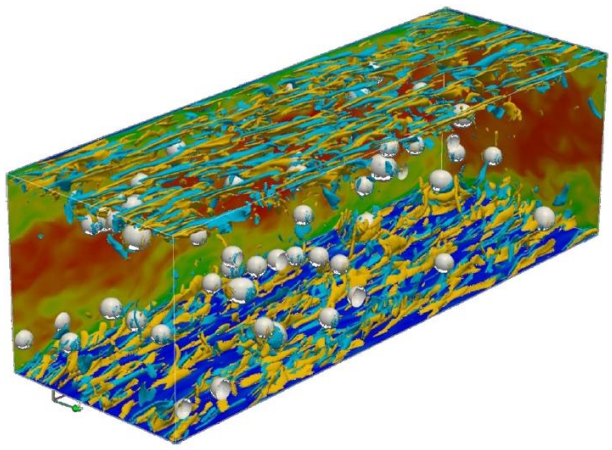

Fig. 1 Turbulent bubble flow simulation by Bolotnov et.al.[2]

By separately analyzing turbulent bubbly flow simulations [2] and the effect of bubbles nucleating on the wall new insight into turbulent boiling phenomena can be obtained. The presented work validates the stabilized finite element code in simulating smooth turbulent channel flows against classic DNS data of Moser et al. [5] for Re_τ = 400 (based on friction velocity). Note that $Re_\tau = 180$ and 395 have been already validated in [6] against the same set of data. For validation purposes rough channel simulations were also carried for rectangular rod type of roughness and are compared against the experimental data of Krogstad et al. [7] and validated numerical results of Ashrafian at al.[8] for rectangular type of roughness (Fig. 2).

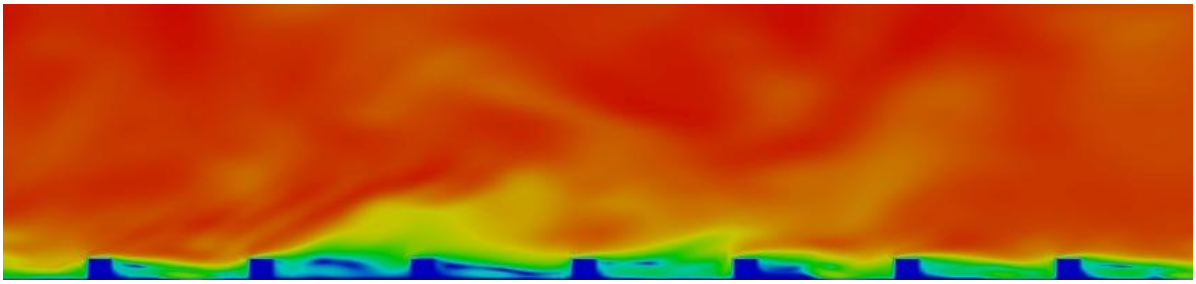

Fig. 2 Rectangular type of roughness in turbulent channel flow

We used a no-slip (zero velocity) condition inside the computational domain to block certain nodes to represent the individual roughness elements here (similar to the approach for hemispherical elements). The same approach is further used in this study to generate five cases of interest: surface roughness represented by uniformly distributed hemispherical roughness elements with varying spacing to model bubbles on the wall (Fig. 3).

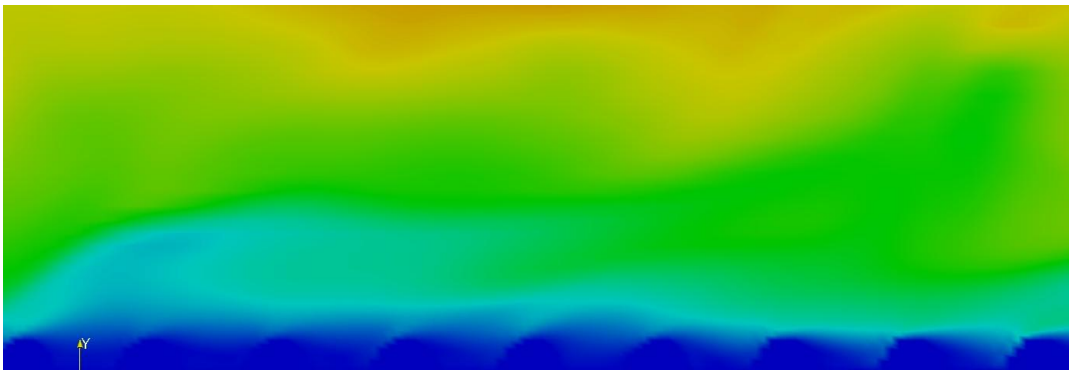

Fig. 3 Rough hemispherical type of elements in turbulent flow

Several measurement probe locations are used to extract mean velocity profiles, turbulent kinetic energy distribution and Reynolds stresses. The effect of different bubble distributions on the mean flow rate was quantified by calculating friction factor for each case. The friction factor is correlated with the bubble nucleation density which in turn is substituted in functions available in the literature relating nucleation site densities to wall heat flux. These have been provided by Klausner and Zeng in 1993 [9] and more recently have been improved upon by Dhir et. al. [10]. Dhir et.al. propose that nucleation site density depends only on wall superheat and contact angle. It is argued that the wall superheat will implicitly take into account the Reynolds number of the flow. Thus Dhir's proposed correlation should be valid for a variety of Reynolds numbers. Using Dhir's correlation and function of friction factor versus the nucleating bubble density we may develop the relation between wall superheat and friction factor in nucleate boiling regimes. This relation will help in generating insight in the effects of nucleating bubbles on turbulent flow. Further the resulting friction factor / wall superheat correlation can be used in generating turbulent

boundary condition in flow boiling regime when near wall behavior is not resolved completely (e.g. for high Reynolds number turbulence models like $k-\varepsilon$ models).

Additional research effort was directed to improve the modeling of deformable bubbles on the wall by using level set interface tracking method. Dynamic contact angle is a local phenomenon which depends upon material properties and flow conditions. Contact angle is an important parameter that affects flow as well as pool boiling. Application of contact angle at a micro level was done by Dhir et.al.[11] for simulating nucleate boiling phenomenon. They refine the simulation domain in the bubble microlayer region to model near wall-bubble interaction. However this might not be practical in production level scenarios. The approach in this study has been to develop a model which allows modeling of this behavior without resolving the bubble microlayer. Previously implementation of fixed contact angle by Renardy [12] has been done in 2001 using Volume of Fluid type interface tracking in 2-dimensions. Studies have also been conducted for implementing a constant advancing and constant receding contact angle by Liu et al. [13]. In this study we use the approach followed by Liu [13] to relate contact angle to contact line velocity. Three types of dynamic contact angle models were tested by Afkhami and Bussman [14] in 2006 using a 3D VOF-based model to simulate a drop impingement on an inclined surface. They suggested that use of different models leads to different fluid deformations. Through this study these models have now been implemented in level set formulation in PHASTA to model contact angle based on contact line velocity.

2. DESCRIPTION OF SIMULATION

DNS Solver overview: PHASTA is a Parallel, Hierarchic, higher-order accurate (from the 2nd to the 5th order accuracy, depending on function choice), Adaptive, Stabilized (finite element) Transient Analysis flow solver (both incompressible and compressible). It has been has been shown by [15] and [16] to be an effective tool for bridging a broad range of length scales in turbulent (RANS, large-eddy simulation (LES), detached eddy simulation (DES), DNS) flows. PHASTA has been used to simulate turbulent flows and validated against various validation benchmarks[17]. The PHASTA code uses advanced anisotropic adaptive algorithms [18] and the most advanced LES/DES models [19]. This capability has been [20] extended to two-phase flows where we use the level set method to track the boundary between two immiscible fluids (either compressible or incompressible – to study bubble coalescence and two-phase turbulence[2, 3]). PHASTA can use anisotropically adapted unstructured grids and regular grids and its highly scalable performance on massively parallel computers has already been demonstrated (the code has shown good scaling out to 288*1024 IBM Blue Gene processors, at JUGENE, BG/P (Germany) [21] and more recently up to 768,000 cores on Mira at Argonne National Laboratory.

2.1 Overview of simulation cases

To generate baseline data against which we may compare the rough wall results a smooth wall simulation was performed (Fig. 4). This also provides a means for validation of PHASTA against results of [7]. For rough wall cases, nucleating bubbles are represented by hemispherical roughness elements placed on the channel wall (Fig. 5). Even though all the

cases under consideration have the same basic flow geometry (flow between parallel plates) they have different meshing requirements due to various wall roughness spacing. Spherical roughness elements are resolved with 8 computational nodes across the diameter. They are arranged in square lattice and rectangular elements are arranged across and running through the channel width perpendicular to flow direction. The latter aids in validating PHASTA results against previously published results [5], [8], [7].

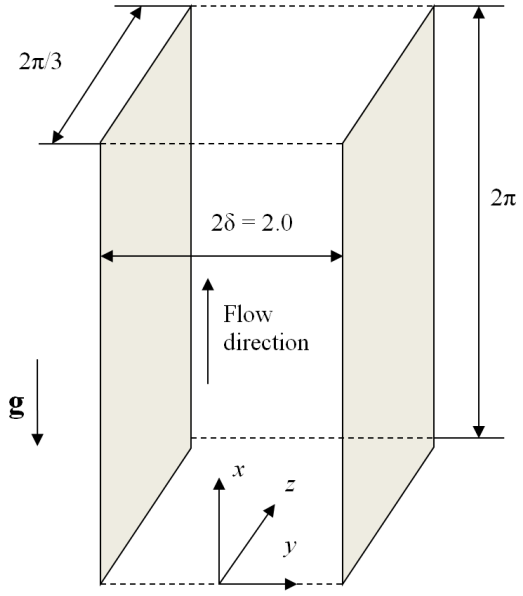

Fig. 4 Simulation domain dimensions and axis orientation (walls are shown shaded)

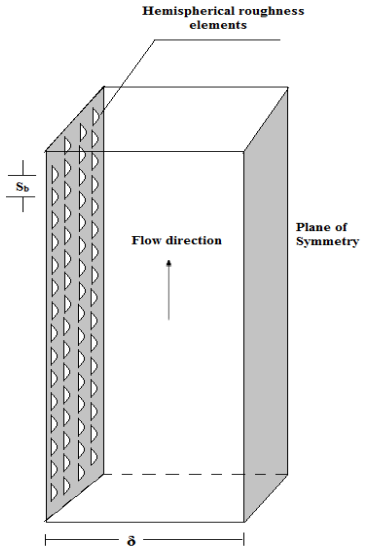

Fig. 5 Simulation domain with roughness elements shown

2.1.1 Smooth Wall

For validation a case for flow between smooth parallel plates was created for which published data exists. For a smooth wall direct numerical simulation (DNS) the turbulence fluctuations are resolved down to Kolmogorov's scale. Typically mesh resolution is expressed in terms of viscous units, which are defined as

$$\Delta x_i^+ = \frac{u_\tau \Delta x}{\nu} \tag{1}$$

Where, ν is the kinematic viscosity, u_τ is the friction velocity:

$$u_\tau = \sqrt{\frac{\tau_w}{\rho}} \tag{2}$$

Here τ_w is the wall shear stress and ρ is the fluid density. To estimate u_τ we used the fixed non-dimensional hydraulic diameter (d_h), $\rho = 1$ and mean velocity ($U_m = 1.0$) to calculate the kinematic viscosity (ν) for a given Reynolds number. Colebrook's equation [22] was used to find the friction factor

$$\frac{1}{\sqrt{f}} = -2\log_{10}\left(\frac{\epsilon}{3.7d_h} + \frac{2.51}{Re\sqrt{f}}\right) \quad (3)$$

Equation (3) is solved iteratively for the friction factor for a smooth wall (zero roughness, ϵ) for the given Reynolds number using Maple®. Given the friction factor and the mean velocity the wall shear can be calculated. Consequently a simple force balance yields the pressure gradient that is required to maintain the prescribed velocity. Once the wall shear was known u_τ was calculated and the friction factor based on u_τ, ($Re_\tau = \frac{u_\tau d_h}{\nu}$) was estimated. The kinematic viscosity was adjusted to obtain the desired $Re_\tau = 400$. Table 1 summarizes the channel flow domain parameters. Note that the normal to the wall resolution (y) is variable to properly resolve boundary layer. The mesh size used for smooth wall simulation is 9.29 million hexahedral elements. In this case the wall has no roughness. Fig. 4 shows a basic schematic of the computational domain. Periodic boundary conditions are applied in x (stream-wise) and z (span-wise) directions. No-slip boundary condition is applied at the walls.

Table 1 Smooth wall simulation mesh parameters

Direction	Boundaries	Number of nodes	Resolution
X	0.0 … 2πh	256	$\Delta x^+ = 9.8$
Y	-1.0h … 1.0h	189	$\Delta y^+ = 0.5 \ldots 5.0$
Z	0.0 … πh	192	$\Delta z^+ = 6.5$

Fig. 6 shows the hexahedral mesh structure designed for the smooth wall simulation with resolved instantaneous velocity field.

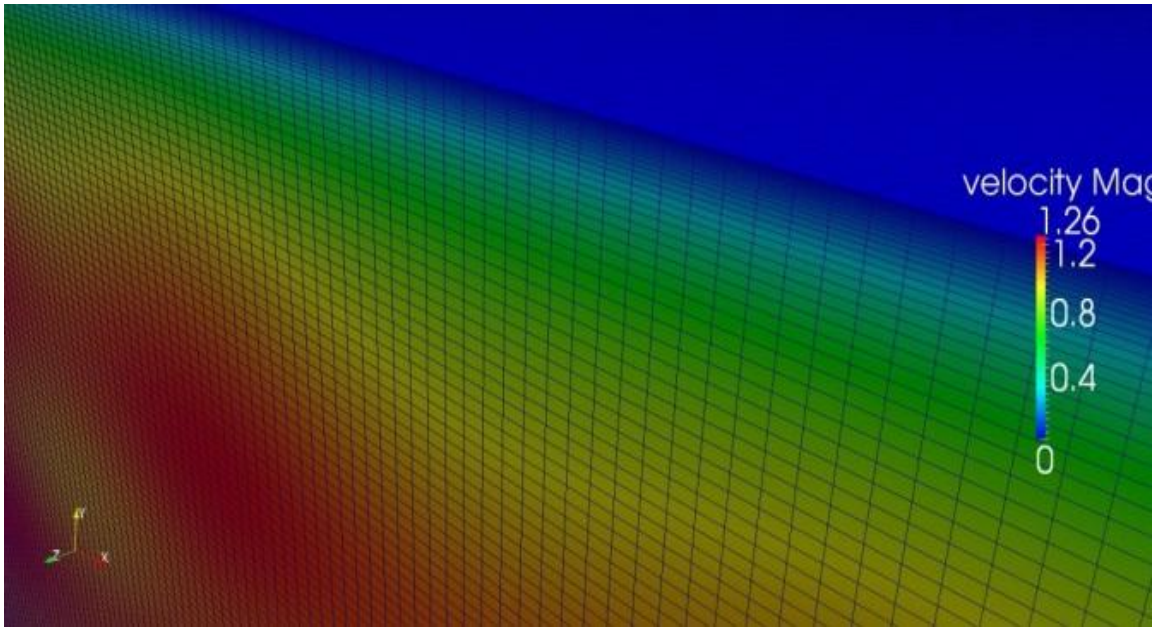

Fig. 6 Part of the simulation domain for smooth wall case. (Velocity magnitude is shown)

2.1.2 Rough Wall

The second case was developed to validate PHASTA abilities in performing DNS of rough wall flows. The wall roughness was designed the same way as in DNS results of Ashrafian et. al. [8] and corresponding experimental study of Krogstad et. al. [7]. The challenge in simulating turbulent flows with rough walls is not only in resolving fine turbulent structures, but also adequately representing individual obstacles which collectively make up the rough wall. Finite-element approach used in PHASTA allows application of no-slip condition to any internal node in the domain (the fluid velocity at a chosen set of nodes can be set to zero). The rough wall flow case geometries are described in Table 2 (S_b is the spacing between the roughness elements).

Table 2 Cases overview (y+ units)

Case	Roughness	Spacing (S_b)	Size (h_b)
Rect	Rectangular	108.8	13.6
A01	Hemisphere	25	10
A02	Hemisphere	32.5	10
A03	Hemisphere	40	10
A04	Hemisphere	60	10
A05	Hemisphere	110	10

In order to properly apply periodic boundary conditions in the stream-wise direction, the domain length has to be revised. This comes from the fact that an integer number of roughness elements should fit in the domain, and uniform spacing between the roughness

elements is maintained throughout the domain. The no-slip condition was applied to represent the roughness elements, mesh resolution can stay the same (in terms of size of computational cells) since each roughness element has the same size in each case and represented by an integer number (8 across diameter) of finite elements in the computational mesh**.** Table 3 presents a summary of the computational domain parameters for a channel with rectangular roughened wall. The mesh size used in the simulation is approximately 22M hexahedral elements. Fig. 7 shows the cross section of a single rectangular roughness element.

Table 3 Rectangular roughness wall simulation mesh parameters

Direction	Boundaries	Number of nodes	Resolution
X	0.0 … 6.528πh	768	$\Delta x^+ = 3.4$
Y	-1.0h … 1.0h	179	$\Delta y^+ = 0.5 \ldots 6.5$
Z	0.0 … πh	160	$\Delta z^+ = 7.8$

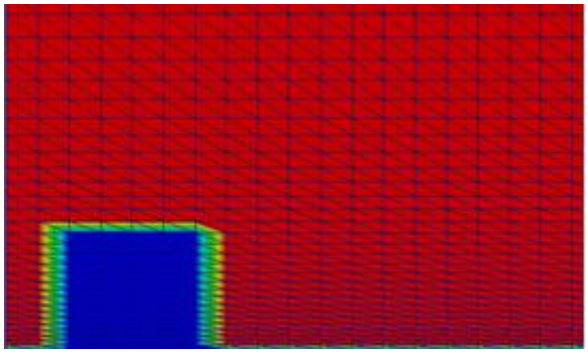

Fig. 7 Side view of a rectangular roughness element with domain grid (hexahedral grid)

2.2 Rough wall channels with hemispherical obstacles

Designing the mesh with hemispherical obstacles proved to be quite challenging since adequate representation of hemispheres by a rectangular grid requires fine grid resolution. Since the domain has periodic boundary conditions the dimensions were adjusted to allow an integer number of roughness elements on the wall in x and z directions.

Table 4 summarizes the meshing parameters for this case. Also, the improved resolution in z direction ($\Delta z^+ = 2.5$ vs. $\Delta z^+ = 7.8$ in rectangular roughness case) substantially increases grid size. Even though the hemispherical obstacles are resolved with just 8 points across diameter, the size of the structured mesh will reach 73.8M hexahedral elements ($992 \times 496 \times 150$). Thus, to keep the computational costs reasonable, half of the domain was split along the symmetry plane between the walls. This resulted in the reduction in the y-direction resolution requirements by a factor of two and overall mesh size came down to 37.4M elements.

Table 4 Hemispherical roughness wall simulation mesh parameters.

Direction	Boundaries	Number of nodes	Resolution
X	0.0 … 6.2h	992	$\Delta x^+ = 2.5$
Y	0.0h … 1.0h	76	$\Delta y^+ = 0.5$ … 6.5
Z	0.0 … 3.1h	496	$\Delta z^+ = 2.5$

The spacing between the roughness elements varies for each hemispherical roughness case. Fig. 8 demonstrates individual hemispherical elements for A02 case (radius= 10y+) and Fig. 9,

Fig. **10**, Fig. 11, Fig. 12 and Fig. 13 demonstrate density of roughness distribution for the different cases for a comparative idea.

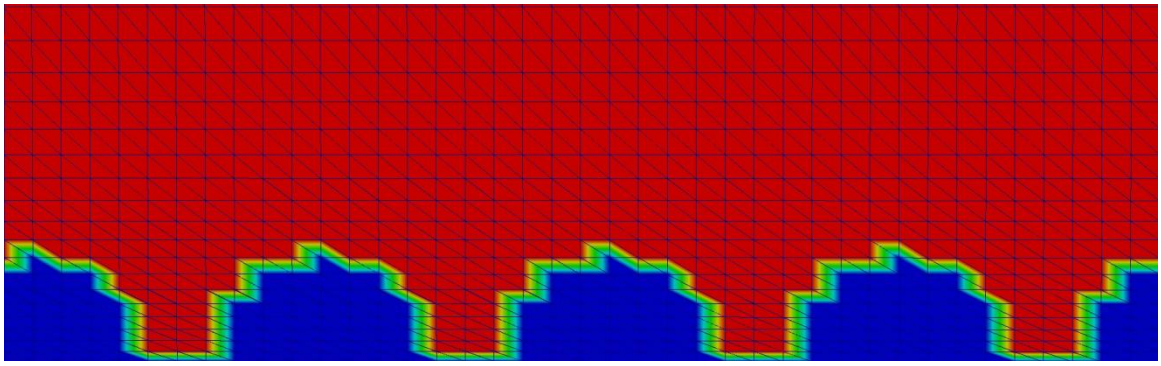

Fig. 8 Hemispherical roughness elements (cross sectional side view for A01 case)

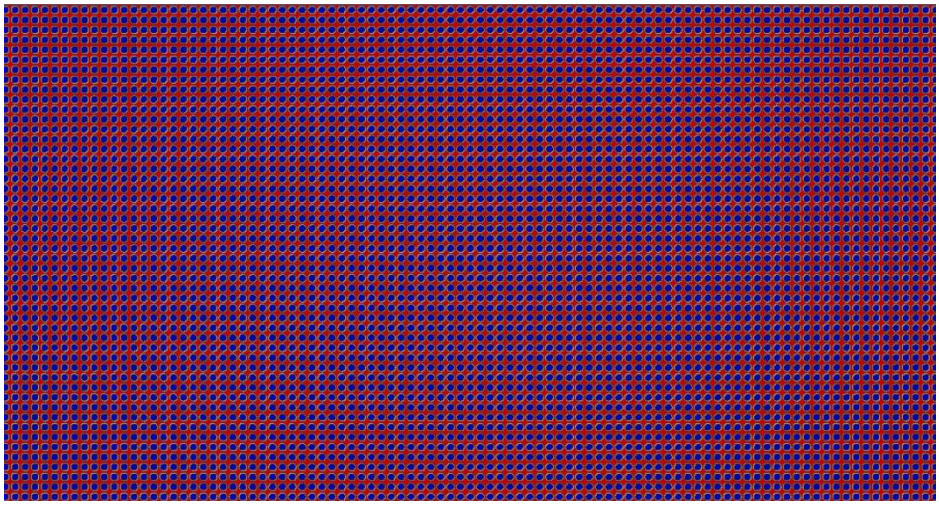

Fig. 9 Top view of roughness element distribution in most dense (A01) case

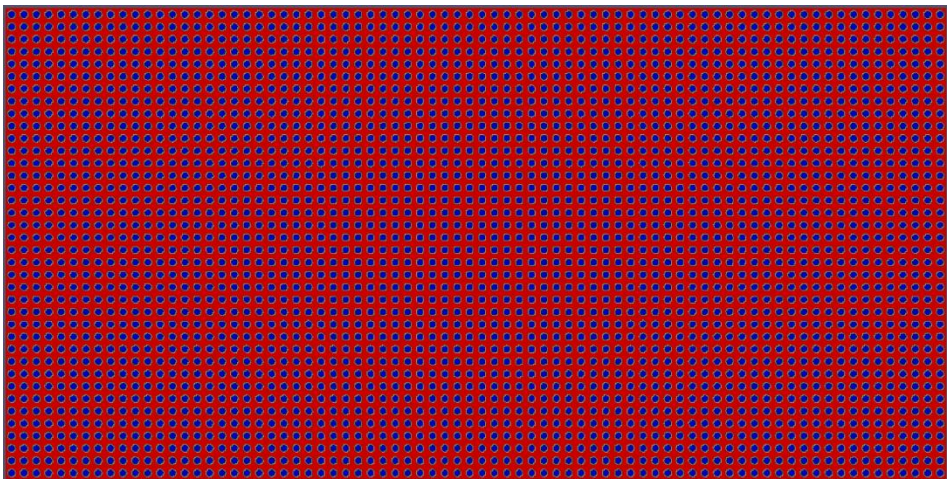

Fig. 10 Top view of roughness element distribution in A02 case

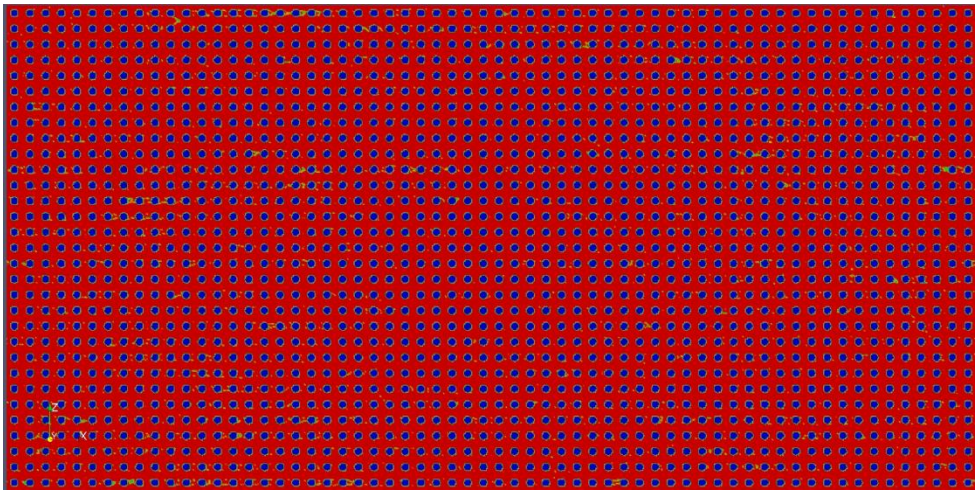

Fig. 11 Top view of roughness element distribution in A03 case

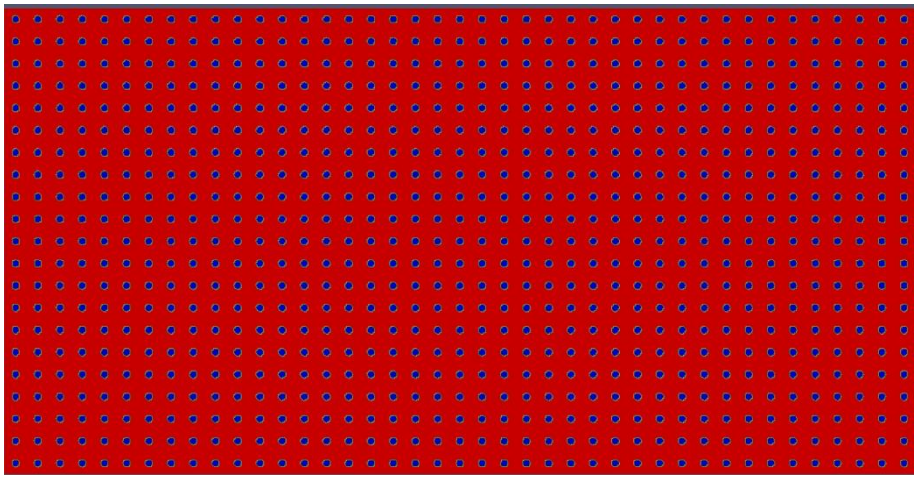

Fig. 12 Top view of roughness element distribution in A04 case

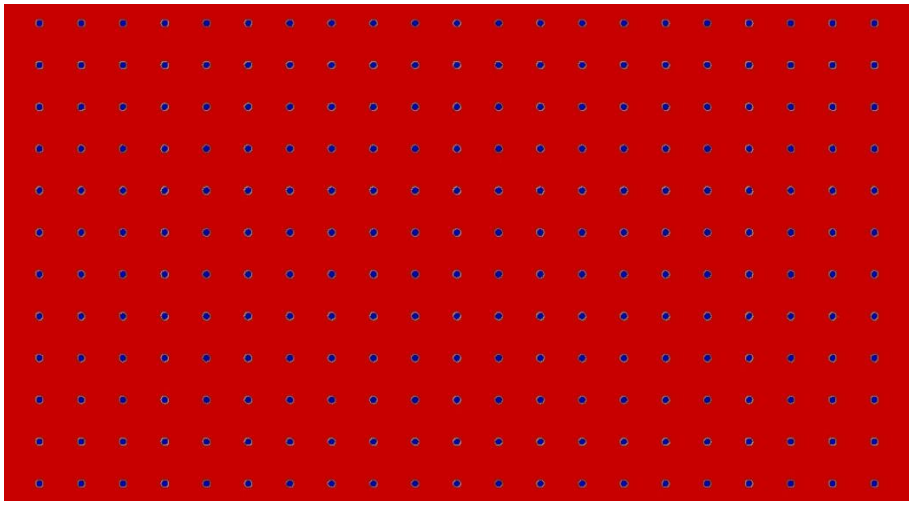

Fig. 13 Top view of roughness element distribution in most sparse (A05) case

2.3 Data acquisition and analysis

PHASTA has a special feature for collecting flow data via virtual probes. These probes can be positioned anywhere in the domain regardless of the actual mesh structure. At the first time step of the simulation each probe location is determined within the finite element mesh and proper weights are computed and stored according to finite element shape

functions values for quick computation of the velocity, pressure and temperature at each subsequent time step.

Additional pre-processing and post-processing is required to obtain meaningful results. The first step is to generate a list of probes where the velocity field will be recorded. PHASTA uses this list to record time history of flow parameters at each probe. For quality turbulent statistics the number of probes can reach 10,000 to 15,000. This is also an approximate upper limit for the number of probes to keep the code performance loss within 10-15%.

2.3.1 Rectangular Roughness Elements

Probe positions for rectangular roughness element case are shown in Fig. 14. Four sets of virtual probes were used to record the flow information in this case. The probes' locations were consistent with the measurements of Ashrafian et al. [8]. The following locations were used: $x/S_b = 0.312$, $x/S_b = 0.71$, $x/S_b = 0.875$, $x/S_b = 1.0$, where S_b is the distance between the roughness elements.

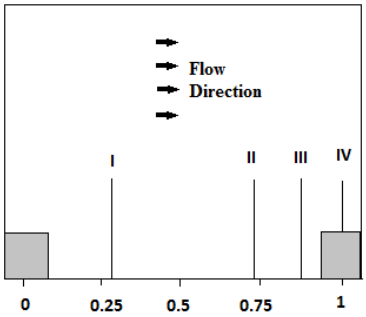

Fig. 14 Measurement station locations with respect to rectangular roughness elements [8].

2.3.2 Spherical Roughness Elements

In order to analyze the detailed flow behavior around hemispherical obstacles, 7 sets of virtual probes were placed in the computational domain (Fig. 15). Spherical roughness elements may be considered to be a first order approximation to nucleating bubbles thus the advanced probe placement presented here will help us in generating data for multiphase modeling in turbulent boiling conditions. We expect to see most of the difference in the region of $y^+ < 50$ (note that the obstacles height corresponds to $y^+ = 10$).

The post-processing step entails analyzing the PHASTA virtual probe data. Major turbulence parameters can be determined using the following set of equations:

$$U_i(t) = \frac{1}{N_e}\sum_{m=1}^{N_e}\left(\frac{1}{N_w}\sum_{j=1}^{N_w} u_m^i(t+t_j)\right) \tag{4}$$

$$k(t) = \frac{1}{N_e}\sum_{m=1}^{N_e}\left(\frac{1}{N_w}\sum_{j=1}^{N_w}\sum_{i=1}^{3}\frac{1}{2}(u_m'^i(t+t_j)^2)\right) \tag{5}$$

where, $u_m'^i(t+t_j) = u_m^i(t+t_j) - U_i(t)$ is the fluctuation of velocity component-*i* computed during the ensemble run *m* at the time instant $t + t_j$; N_e is the number of ensemble runs, N_w is the number of velocity samples in each window, *t* is the current time, $t_j = (j - N_w/2)\Delta t$ is the local window time, and Δt is the time step.

To ensure the convergence of the statistics obtained by the above data acquisition technique, results from two consecutive time windows were individually averaged and

compared. The quantity of interest is determination of wall shear parameter in terms of friction factor as a function of roughness density. For this the following equation is used:

$$f = 8h\frac{\left(-\frac{dp}{dx}\right)}{\rho U_m^2} \qquad (6)$$

where h is the 1/4th of hydraulic diameter (and corresponds to channel half-width). A deviation up to about 5% of mean velocity in stream-wise direction in successive time windows was considered to be sufficient for the scope of this study. Fig. 15 shows the top view of the probes as they are placed with respect to the spherical roughness elements. In A02, A03, A04 and A05 cases d has been taken to be diameter of the roughness elements i.e. $d = dia_{roughness}$. However in A01 (most dense) case the bubbles are so close together that the probe locations situated at d distance from center actually overlap with the next bubble (Fig. 16). In this case the d used is half the distance between the bubbles, i.e. $d = \frac{S_b}{2}$ such that probes 2 and 3 lie in the centre of gap between consecutive bubbles and probe 4 lies in the center of the void between four adjacent bubbles Hence the probes 3 and 4 for A01 are located in between the bubbles; probe 4 is in the center of four adjacent bubbles.

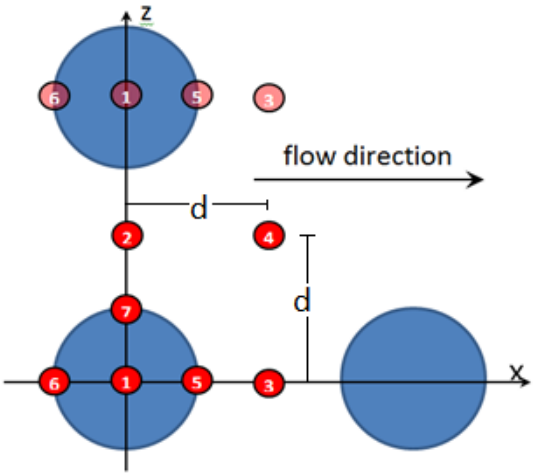

Fig. 15 Location of 7 virtual probe sets in the hemispherical roughness case

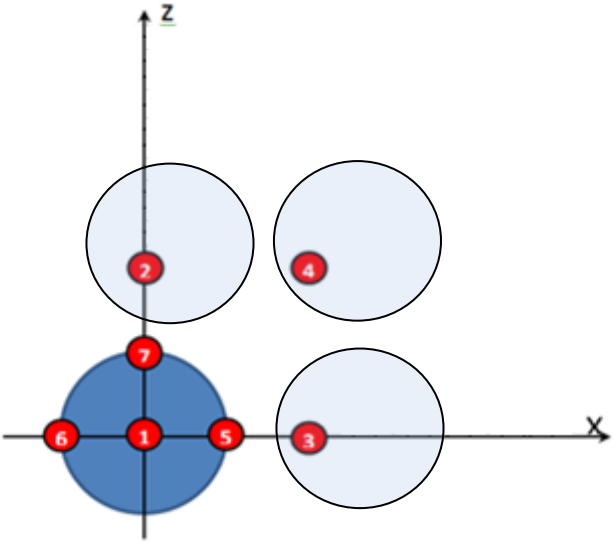

Fig. 16 Probe locations overlap with roughness elements in A01 case.

3. RESULTS AND DISCUSSION

Results for channel with smooth wall [5] and rectangular roughness elements [7],[8] are used as benchmarks to validate the performance of the finite element solver (PHASTA) used in this work.

3.1 Validation Case: Smooth Wall

Full domain (two walls) smooth wall simulation was performed for 51,500 time steps. The presented statistics was collected over the last 8,340 time steps. The mean velocity profile is compared with the law of the wall, Fig. 17:

$$U^+ = \frac{1}{\kappa}\ln y^+ + B \tag{7}$$

where, $\kappa = 0.4$ and B = 5.8. We also show the laminar sublayer law of $U^+ = y^+$, which is expected to be valid for $y^+ < 5$.

3.2 Validation Case: Wall with Rectangular Roughness

Full domain (two walls) rough wall simulation was performed for 31,500 time steps. The presented statistics were collected over the last 3,300 time steps and was also compared with the next-to-last time windows of the same width to ensure that the solution is converged. Fig. 18 shows the evolution of mean velocity and turbulent kinetic energy (TKE) profiles at measurement station 2 averaged at two consecutive time windows to ensure statistical convergence for rectangular roughness case. Note that TKE is not fully converged.

Longer simulations are required to provide quality statistics for higher order terms such as turbulence production, dissipation and diffusion.

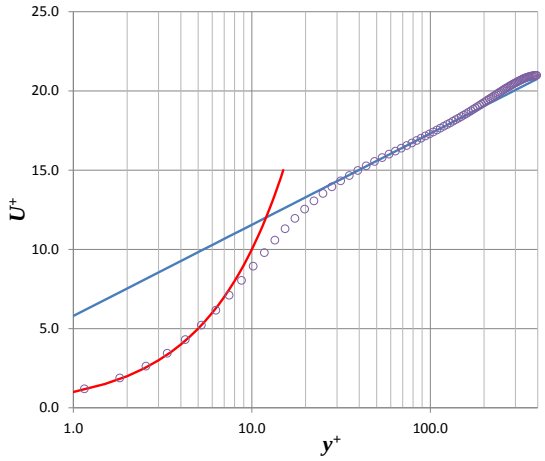

Fig. 17. Smooth wall channel flow compared with the law of the wall (solid lines). PHASTA results are shown with circles.

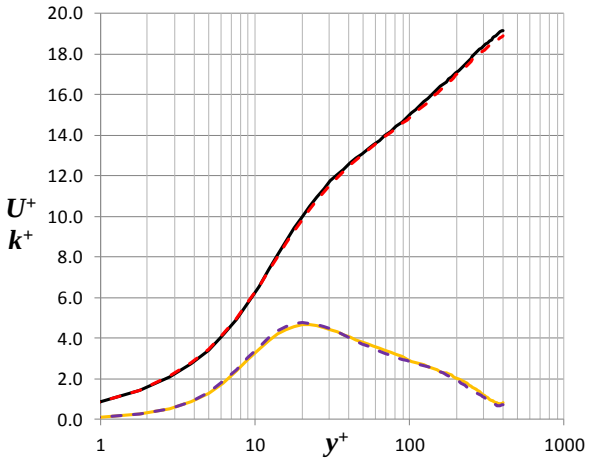

Fig. 18. Comparison of mean velocity and turbulent kinetic energy (rectangular roughness case) for two consecutive time averaging windows.

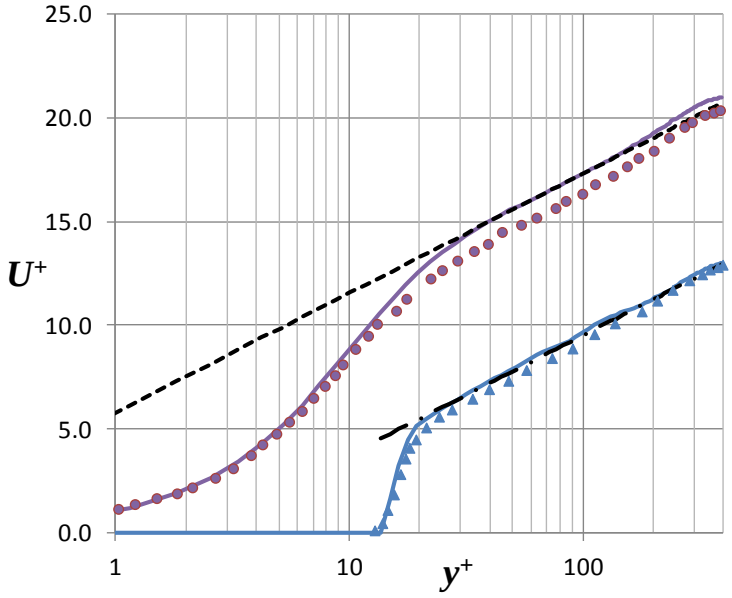

Fig. 19. Mean velocity profiles in inner coordinates for smooth and rough (rectangular roughness elements) channel flow simulations by PHASTA (violet and blue solid lines) and DNS results by [7] (symbols).

Fig. 19 shows the law of the wall plot of PHASTA results for both smooth and rough channels compared with data of [7]. For a constant pressure gradient used in both simulations we observe a decrease in average velocity due to roughness, as expected. The log-law region is shifted according to the law-of-the-rough-wall

$$U^+ = \frac{1}{\kappa}\ln y^+ + B - \Delta U^+ \tag{8}$$

where, ΔU^+ is roughness function which quantifies the increase of local drag due to roughness. Bakken & Krogstad [23] suggested the following correlation for the roughness function,

$$\Delta U^+ = \frac{1}{\kappa}\ln \kappa^+ + C \tag{9}$$

where, C = 1.9 for rod-roughened flows. This formula results in estimated value of ΔU^+ = 8.3 for the case under consideration [8]. Our results give the value of 7.8 and [8] obtained value of 7.0. Note that we obtain good agreement with the previous results.

Fig. 20 shows mean velocity profiles at the 4 stations. We can observe a zero velocity at station 4 below the roughness height, as well as backflow at stations 2 and 3 for $y^+ < 6$ and at station 1 at $y^+ < 9$. This is consistent with the results observed by [8].

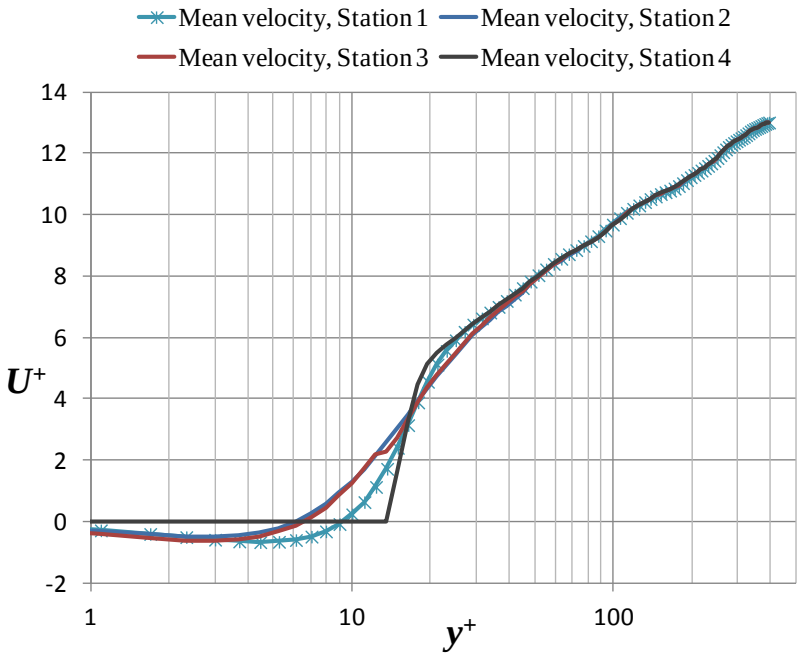

Fig. 20 PHASTA results of inner scaling mean velocity profiles at 4 stations shown in Fig. 14 for the rectangular roughness case.

3.3 Hemispherical Roughness Channel Case

Three cases for hemispherical roughness were analyzed for various bubble densities as given in Table 2. Table 5 presents the statistical sample sizes and simulation times for the three cases.

Table 5 Statistical sample size summary.

Case	Total simulation steps	Time steps used for averaging for statistics
A01	76,600	10,200
A02	51,550	7,808
A03	39,900	4,700
A04	75,750	8,972
A05	34,200	5,696

The results were also compared with the next to last time window of the same width to ensure that the simulation has achieved fully developed, statistically steady-state conditions. Fig. 21 gives an example of the length of time the data is averaged over to produce smooth statistics. The comparison between statistics produced by averaging is shown for the rectangular roughness case in Fig. 18 and for A03 case in Fig. 27.

Table 6 shows the mean velocity deviation for all five cases between the last three averaging windows. The cause of deviation may be explained by the example of the velocity signal shown in Fig. 21 and the large Eddies visible in the cross section of flow field in Fig. 22. Due to large time scale of these evolving eddies different averaging windows will not

give the exact same mean velocity. The long time scale evolution of large turbulent structures in the flow influence the flow and affect the mean velocity data gathered over different times leading to an uncertainty in the overall mean velocity calculation.

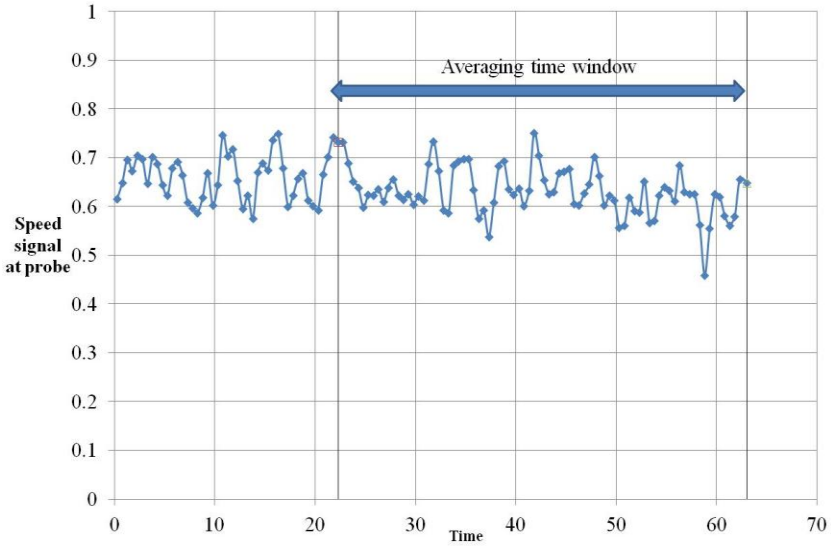

Fig. 21 Example of data averaging window (average velocity over time)

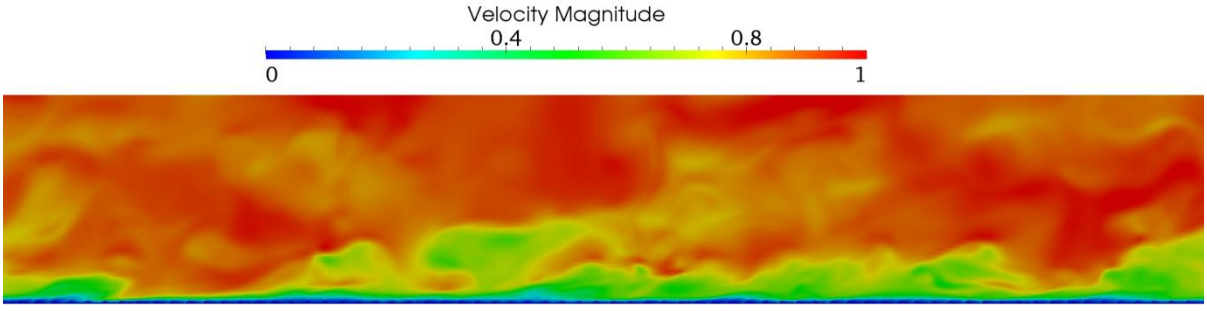

Fig. 22 Cross section of velocity field for A02 case (small roughness elements are visible at the bottom wall)

The mean stream-wise velocity was calculated by averaging the velocity calculated for station 2 along the y direction. This was done using the following equation: (n_p is the probes in the normal to the wall direction which is 76 in our case)

$$U_m = \frac{\sum_{i=1}^{n_p} \Delta y_i U_{i,station=2}}{\sum_{i=1}^{n_p} \Delta y_i} \quad (10)$$

Table 6 Standard deviation in mean velocity

Case	Window 1	Window 2	Window 3	% Standard deviation
A01	0.878	0.854	0.829	2.849
A02	0.813	0.797	0.789	1.530
A03	0.876	0.867	0.867	0.589
A04	0.882	0.906	0.896	1.351
A05	0.925	0.931	0.925	0.416

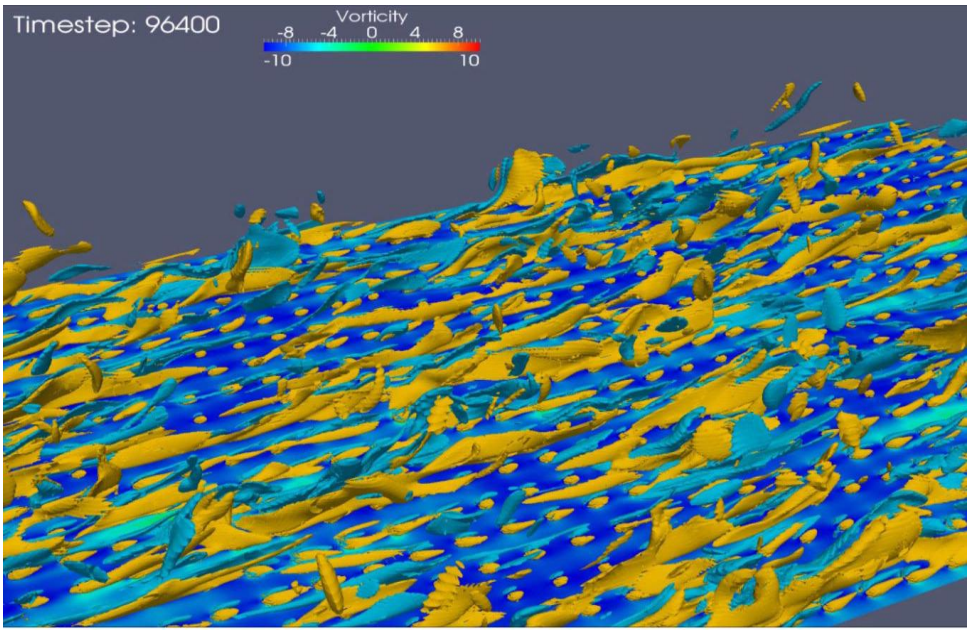

Fig. 23. Y-Component of vorticity induced by the roughness elements (A03 case)

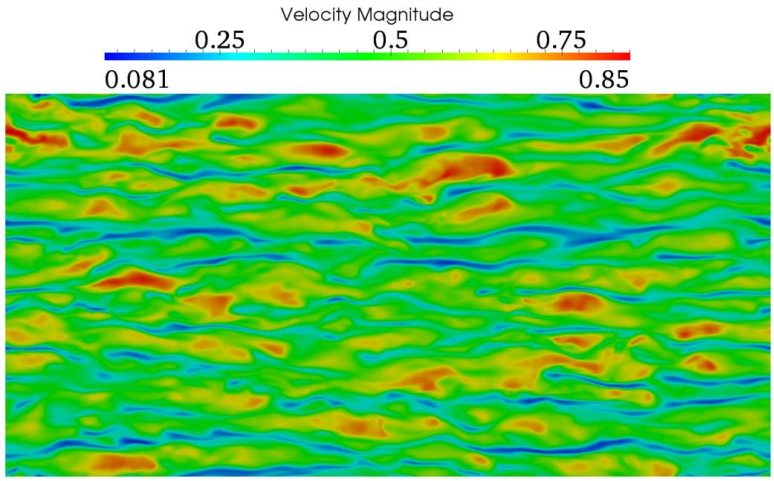

Fig. 24 Near wall velocity field above the roughness elements (A02 case)

Fig. 23 shows the Y component of vorticity, which is $(\boldsymbol{\nabla} \times \boldsymbol{V})_y$ $(or, -\left(\frac{\partial V_z}{\partial x} - \frac{\partial V_x}{\partial z}\right))$. Fig. 23 and Fig. 24 show how the vorticities and turbulent eddy structures tend to align with the

roughness elements. This explains the different nature of turbulence observed in the five cases as the configuration of roughness elements varies.

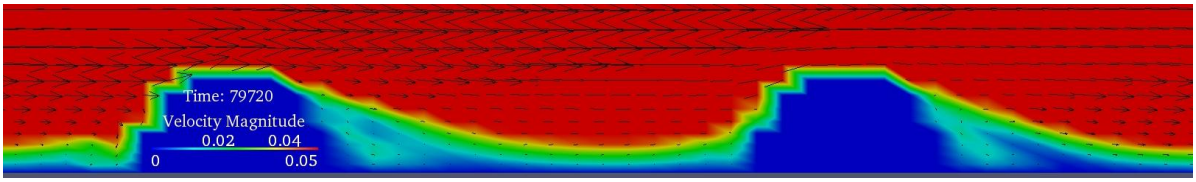

Fig. 25 Velocity vectors for A04 case

Further, Fig. 25 shows a recirculation region being developed behind and in front of the roughness elements for A04 case. This is expected, however as we can see in the next figure (Fig. 26) in the A02 case that as the roughness elements get closer together the recirculation regions merge together and form a larger recirculation region.

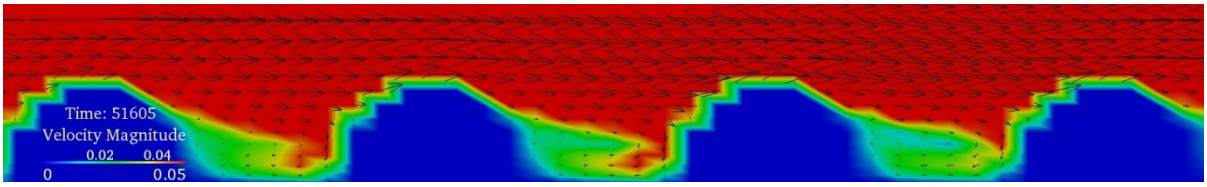

Fig. 26 Velocity vectors for A02 case

This effectively changes the near wall flow behavior and is the cause of different flow physics observed in the cases as the density of roughness varies.

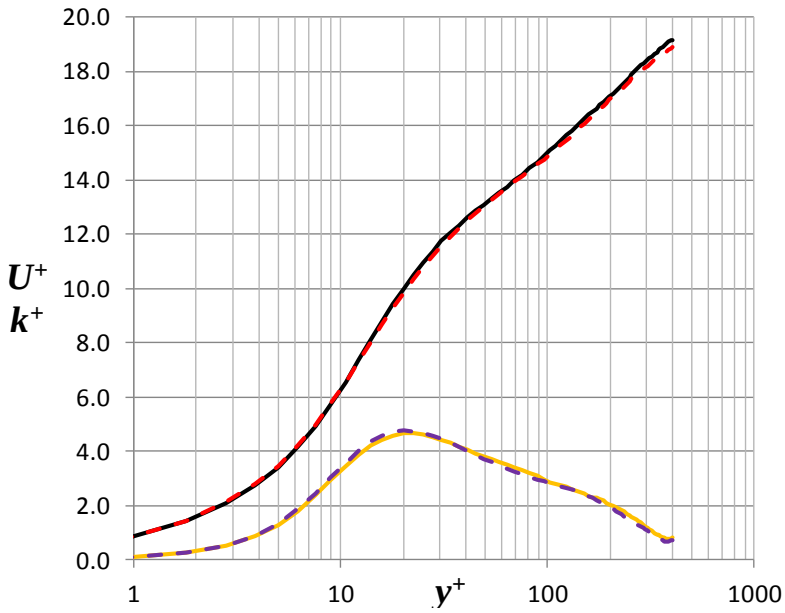

Fig. 27 Successive evolutions of mean velocity and turbulent kinetic energy profiles at measurement station 2 averaged at two consecutive time windows to ensure the statistical convergence for case A03.

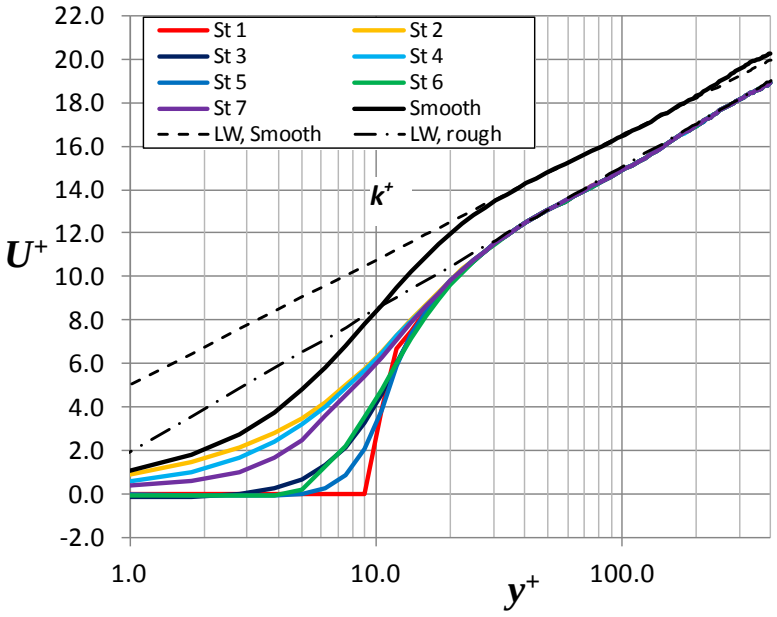

Fig. 28 Mean velocity profiles at different measuring stations compared with the smooth wall result and the law of the wall plots for A03 case.

Measurements were performed at the 7 stations (Fig. 15), and the mean velocity profiles demonstrate the effect of the roughness elements on the flow at each probe location along the wall-normal direction (Fig. 28). We can see that the station #1 has zero velocity up to the height of the roughness elements ($y^+ = 10$). Comparative velocity and TKE profiles for four cases are shown in Fig. 29 and Fig. 30. Based on the figures we might notice that the velocity profiles are affected by roughness density in a non-monotonic fashion. The velocity profiles of A02, A03, A04 and A05 shift upward progressively as the roughness density decreases from A02 to A04. However as the roughness density decreases from A01 to A02 it can be seen that the velocities above 20y+ are higher in A01 case. This suggests that the flow is being affected by the higher roughness density in a manner which reduces overall wall shear on the flow. Further, the plot of non-dimensional turbulent kinetic energy shows that its peak shifts away from the wall (Fig. 29) as the roughness density increases. This may be explained by the fact that as the distance between roughness elements decreases the turbulent flow structures that are generated by the wall are suppressed. Thus the overall TKE peak shifts upwards where the roughness elements don’t block the flow structures (Fig. 23).

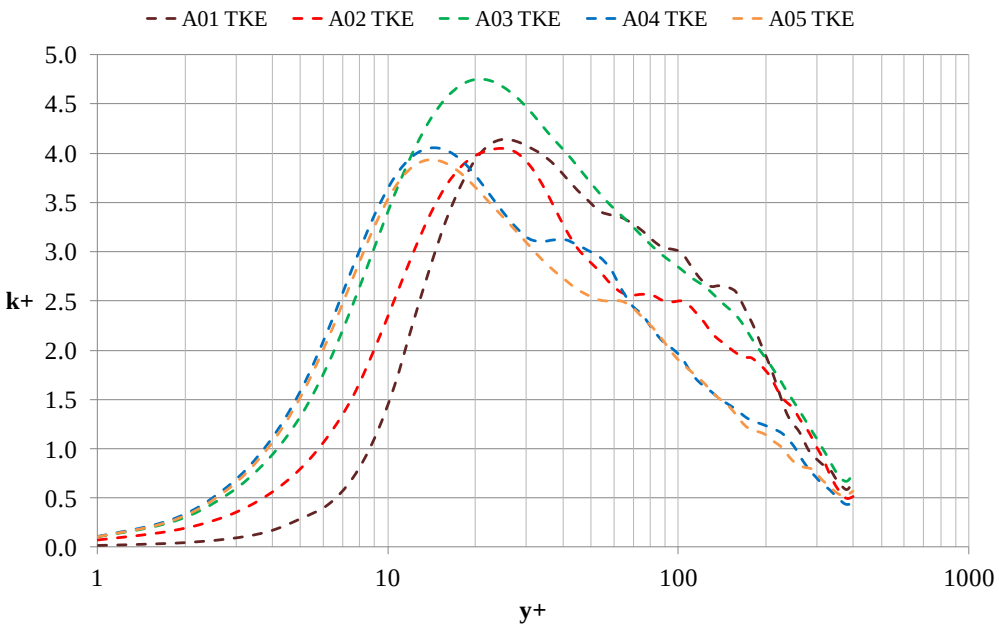

Fig. 29 Comparison of TKE profiles in wall coordinates for the five roughness cases under investigation.

As was demonstrated earlier in the case of rectangular roughness channel, the law of the wall changes considerably in presence of wall roughness (Fig. 20). To measure the effect of roughness density U^+ and y^+ were plotted on a logarithmic scale compared with the law of the wall in Fig. 30. It may be seen that A02 case has the curve which is below A01, A03, A04 and A05. The values of κ and B of the obtained Law of the rough wall are presented in Table 7.

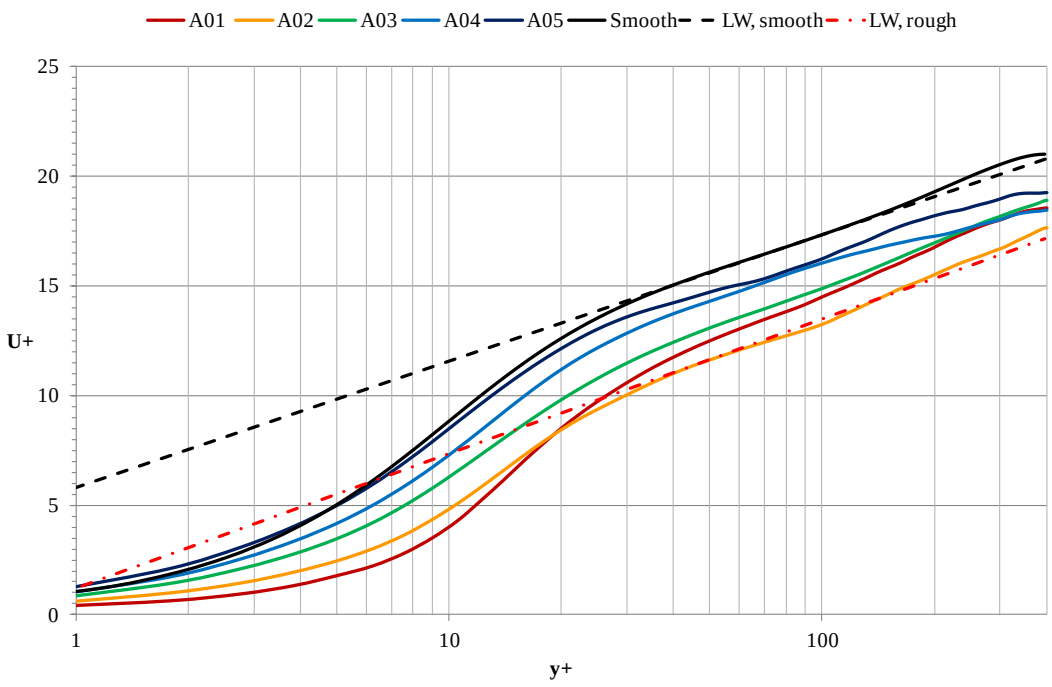

Fig. 30. Effect of roughness on law of the wall. Black lines show the smooth wall result.

Table 7 Law of the rough wall constants.

Case	κ	B
A01	0.34	1.0
A02	0.375	1.2
A03	0.36	2.1
A04	0.36	3.4
A05	0.4	4.78
Smooth	0.4	5.8

It may be observed that the velocity profiles for all the cases are tending to merge together at higher y+ range. This is quite reasonable and may be explained by the fact that as distance from the wall becomes larger the effect of the roughness elements on the flow becomes smaller. From the values of κ and B it may be seen that the different roughness element spacing produce different wall shear rates and thus alter the constants of law of the wall. No particular trend is observable in the κ with respect to the roughness density however a clear trend emerges for B versus roughness density.

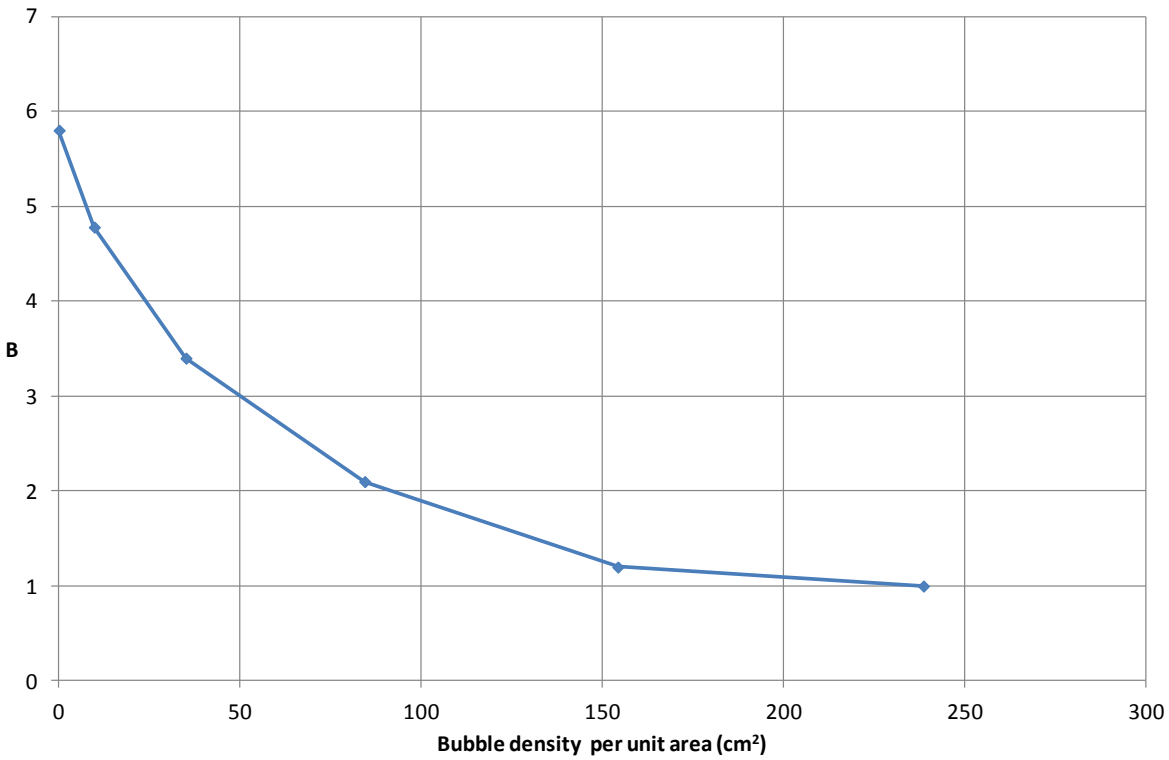

Fig. 31. B versus roughness density.

As the B curve flattens out it suggests that B will attain a minimum value for a particular roughness density. Further it may be argued that as the roughness density tends to a very high number the roughness elements will start to merge with each other and eventually they will smoothen out the wall. Thus it is expected that B will attain a minimum value. As the roughness elements merge together completely and essentially create a smooth wall we also expect to see a maximum in the friction factor with respect to roughness density.

3.4 Friction factor

To study the behavior of friction factor with respect to roughness density it was calculated from the numerical data and is plotted as a function of the roughness element density (Fig. 32). Friction coefficient was estimated using Eq. (6). Considering the smooth wall conditions with Re_D = 29,500 (based on hydraulic diameter, corresponds to Re_τ = 400) the Moody's diagram friction factor estimate is 0.024. The obtained DNS based result for smooth wall is f = 0.02419.

For the rectangular roughness case, $\frac{\epsilon}{d} = 0.0085$; Re_D = 17,000 (based on hydraulic diameter, and computed velocity) the Moody's diagram friction factor estimate is 0.039. The obtained DNS based result is f = 0.071 for rectangular roughness case. This result compares very well with the values reported by [7]: 0.073 for DNS and 0.079 for experiments. This demonstrates that not only the height, but the shape of roughness elements has critical importance on the friction factor.

For the hemispherical roughness cases (A01, A02, A03, A04 and A05) the friction factor was also estimated. Considering the rough wall conditions with roughness; $\frac{\epsilon}{d} = 0.00625$; Re_D = 26,000 (based on hydraulic diameter, and computed velocity) the Moody's diagram friction factor estimate is 0.035. Note according to Moody's chart this value is independent of the density of roughness elements. The obtained DNS based result is f = 0.0347 for A01, f = 0.0379 for A02; f = 0.0314 for A03, f = 0.0293 for A04 and f= 0.0278 for A05, (plot shown in Fig. 32). Table 8 gives the friction factor with the uncertainties. The uncertainty in friction factor may be attributed to the variation in mean velocity. By the formula for propagation of uncertainty we have:

$$\sigma_f^2 = \sigma_{U_m}^2 \left(\frac{\partial f}{\partial U_m}\right)^2 \tag{11}$$

$$\sigma_f = \frac{2f}{U_m}\sigma_{U_m} \tag{12}$$

Substituting values from Table 6 and Eq. (6), (11) and (12) the friction factor and the uncertainty may be found out (given in the following table).

Table 8 Calculated friction factor.

Case	Friction factor (f)	Uncertainty
A01	0.033	0.002 (5.70%)
A02	0.038	0.001 (3.06%)
A03	0.0314	0.0004 (1.18%)
A04	0.029	0.001 (2.70%)
A05	0.0278	0.0002 (0.83%)

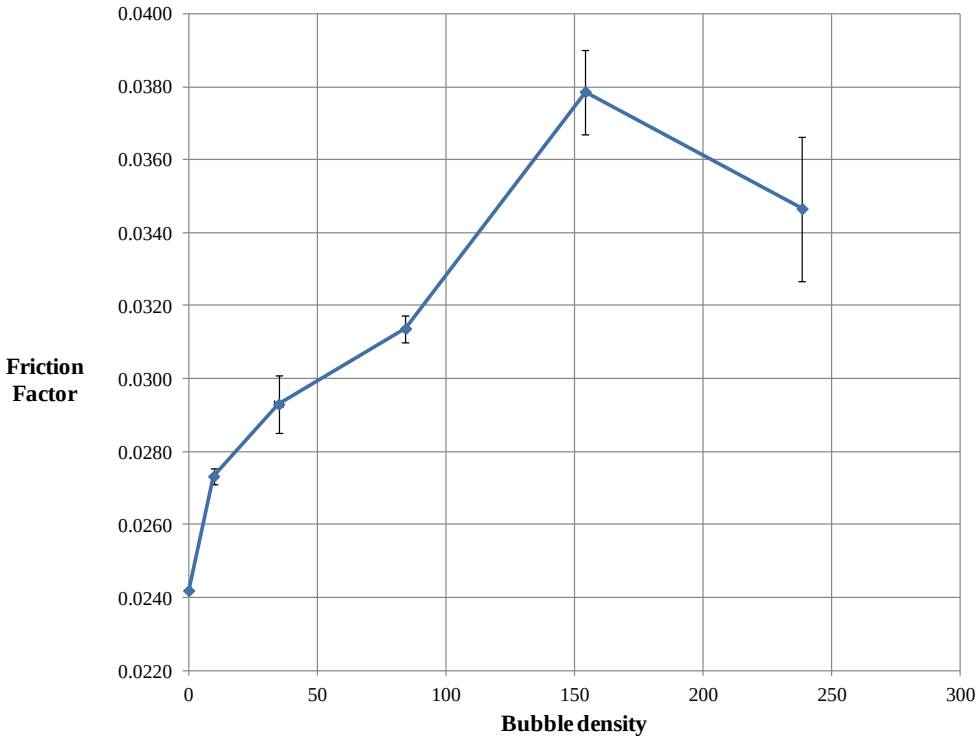

Fig. 32 Friction factor with respect to number of bubbles per cm^2 (with observed error of 0.83 to 5.7%)

Clearly as expected a maximum in friction factor is observed. Further it must be noted that as the roughness density tends to infinity the wall must essentially become smooth as the roughness elements merge into one another (Fig. 33).

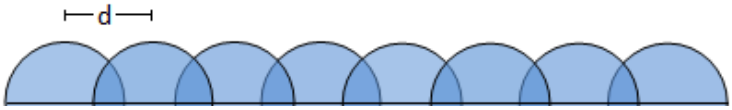

Fig. 33 Roughness elements merge as distance approached the roughness element diameter.

By this argument, we may get one more data point. Since infinity cannot be plotted, it was assumed that the behavior of the wall with infinite nucleating bubbles might be close to a wall with bubbles whose centers are at a distance equal to 1 radius (10y+) and hence have already merged together. By plotting an overall shape of the friction factor function as obtained and which was fitted with a function (Fig. 34).

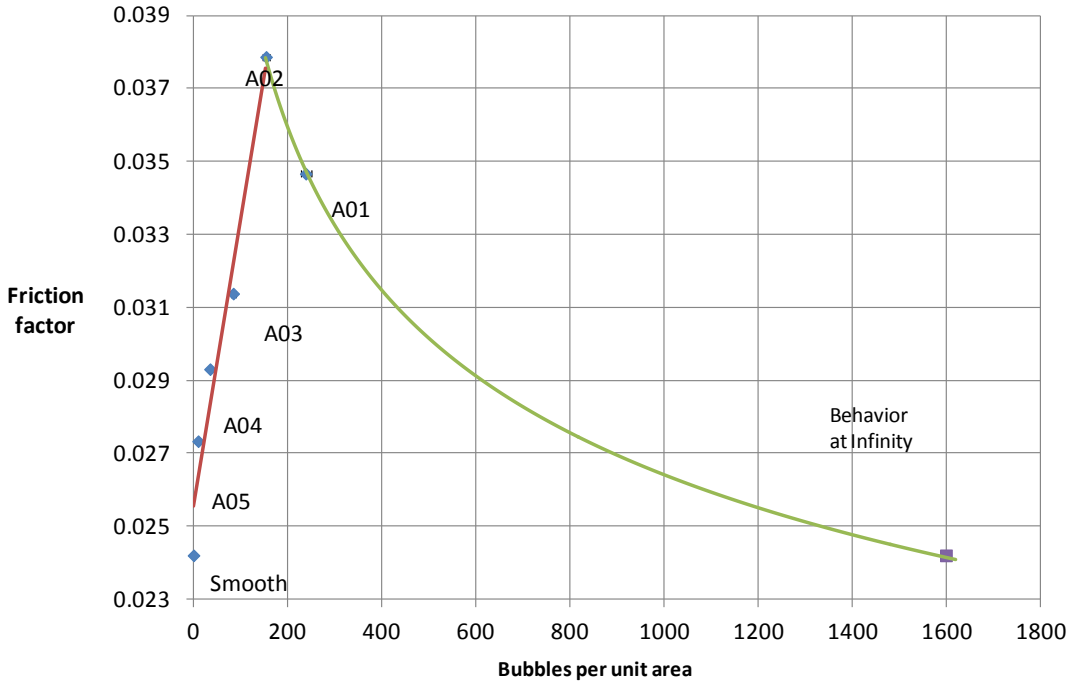

Fig. 34 Friction factor-roughness density function (number of bubbles per cm^2)

Friction factor function is given by the following piecewise equation as a function of density (d is the number of bubbles per cm^2).

$$f = \begin{cases} 7.9158 \times 10^{-5} d + 0.025534 \, , d < 152 \\ 0.0988 d^{-0.191} , d > 152 \end{cases} \quad (13)$$

3.5 Correlation between heat flux and friction factor in subcooled boiling regime

During subcooled nucleate flow boiling in heated channels the bubbles at the wall surface can be approximated as roughness elements at the wall. To understand what effect

these bubbles have on the flow one must model the bubbles. Given the limited resources in this work the bubbles have been approximated as rigid non-moving roughness elements. This approximation was used to quantify the effect of nucleating bubbles on the turbulence. For application of the previously obtained correlation the surface tension forces of the vapor-water-wall interface must be strong enough to keep the bubble from either moving or deforming.

When the bubbles behave nearly rigid and stationary the function of friction factor with respect to roughness (bubble) density (Fig. 32) can be applied at the wall in conjunction with the heat flux associated with that particular nucleating bubble density. The correlation between heat flux and friction factor for subcooled flow boiling is given by Dhir et. al.[10] for a range of inlet subcooling and contact angle values in the turbulent flow regime as given in Eq. (14).

$$d = \begin{cases} 0.34(1-\cos(\Theta_s))\Delta T_w^{2.0}\,, if\ \Delta T_{w,ONB} < \Delta T_w < 15^o \\ \\ 3.4\times 10^{-5}(1-\cos(\Theta_s))\Delta T_w^{5.3}\ \ , if\ \Delta T_w > 15^o \end{cases} \tag{14}$$

where, $\Theta_s$is the contact angle and ΔT_w is the wall superheat. These equations may be used with equation (9) to obtain a correlation between wall superheat and friction factor. Using (13) and (14) we get (for a contact angle of 90^o),

$$f = \begin{cases} 2.6914\times 10^{-5}\Delta T_w^{2.0} + 0.025534\,, \Delta T_w < 15^o C \\ 2.6914\times 10^{-9}\Delta T_w^{5.3} + 0.025534\,, 15^{\circ}\mathrm{C} < \Delta T_w < 18^o C \\ 0.70509\Delta T_w^{-1.0123}, \Delta T_w > 18^o C \end{cases} \tag{15}$$

Fig. 35 shows the plot of proposed fit (i.e. Eq.(15)) with the plot of the observed friction factor as a function of the wall superheat.

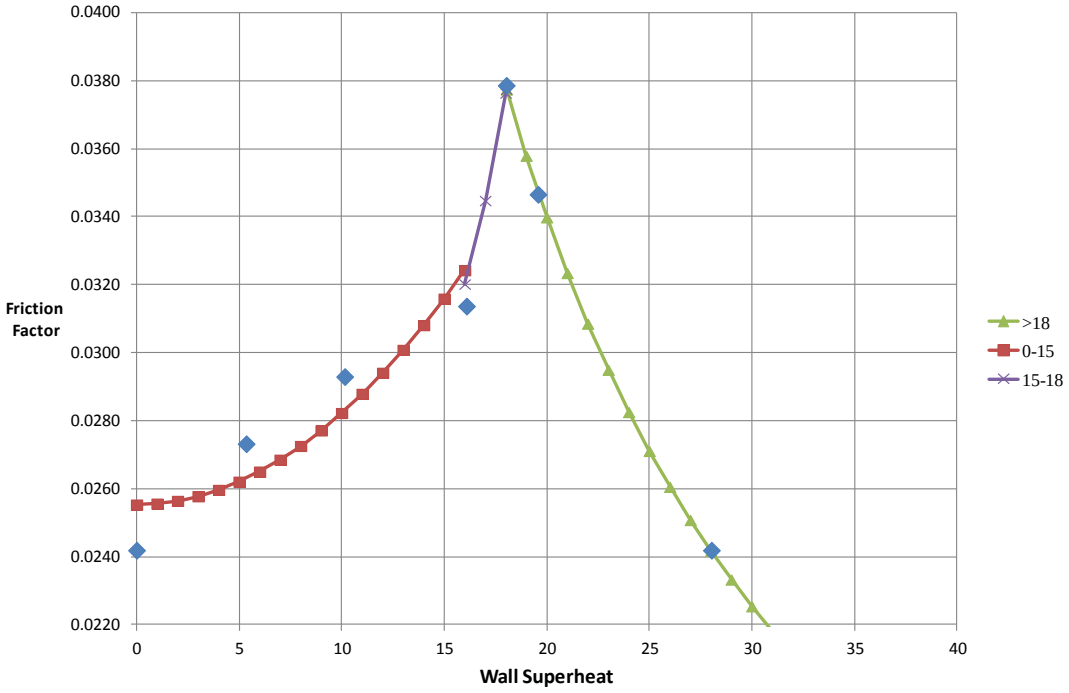

Fig. 35 Friction factor versus wall superheat

The proposed correlation uses the nucleation site density to the wall superheat dependency proposed by Dhir et.al. [10] which was reported to have an accuracy of $\pm 40\%$. The friction factor – nucleation site density correlation has an error range of $0.83\% - 5.7\ \%$. Since both the steps of relating nucleation site densities to wall superheat and friction factor to nucleation site density are independent, it may be thus inferred that correlation proposed in Eq. (15) thus has an overall uncertainty of $\pm 43.3\%$. Using Eq. (15) we can modify the

boundary conditions for CMFD simulations for boiling flows in using high Reynolds number $k-\varepsilon$ models.

4. APPLICATION OF INTERFACE TRACKING FOR BUBBLE ON WALL

Fig. 36 shows the schematic of the contact forces that act on a bubble. A spatially varying force is applied in a force application region (FAR) around the interface which acts as the contact force. The requirement is to apply a numerical force in order to achieve the prescribed contact angle.

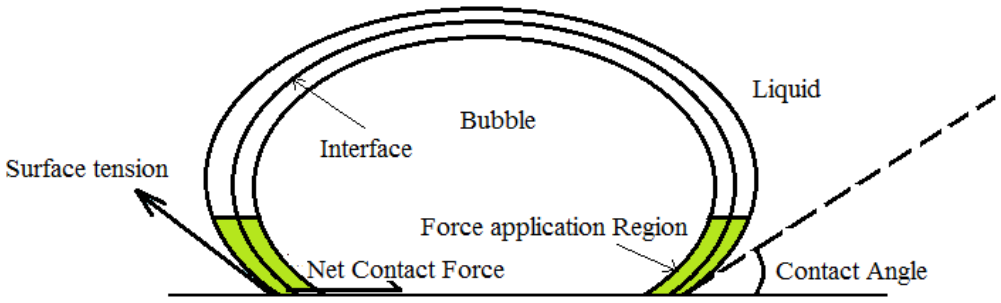

Fig. 36 Contact force schematic and force application region

The model testing was performed on a sample case representing a single bubble sitting on a wall. The initial condition for the simulation is shown in Fig. 37. The simulation domain was 20x10x10 $[mm^3, mesh\ size = 100 \times 100 \times 100]$ with bubble radius of 2.5 [mm]. The initial level set distance field represents a semi-spherical bubble and is given by the following equation:

$$\phi = \sqrt{(x - 0.01)^2 + (y + 0.005)^2 + (z - 0.005)^2} - 0.0025 \qquad (16)$$

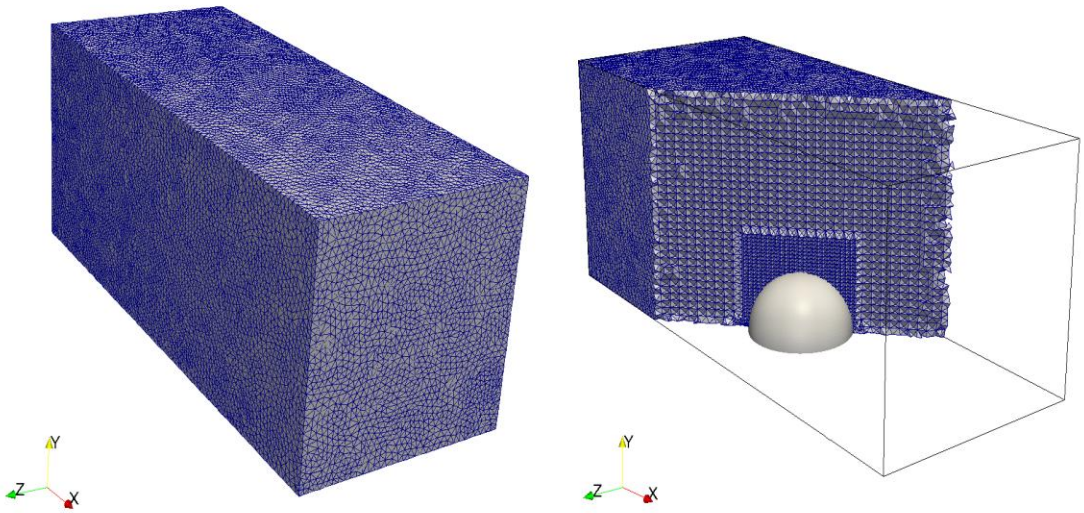

Fig. 37 Simulation domain and bubble

4.1 Contact Angle Control Algorithm

The contact angle control algorithm involves application of a force which has dependence on three parameters:

- deviation of contact angle from true value ($\Delta\theta$)
- distance from interface (ϕ)and
- distance from wall (d_{wall}).

The respective components of the contact force have been named F_1, F_2, F_3 respectively. The contact force varies smoothly in space and with the difference between the current and the

desired contact angles. The proposed functional dependence of contact force on contact angle is given as following:

$$F_1 = K\left(\frac{1}{2} + \frac{1}{\pi} * \text{atan}\left(\frac{\Delta\theta - M_{adv}}{S}\right) - Y_{adv}\right) \quad (17)$$

where, $K = 8\times10^6$ is a model constant, M_{adv} is the offset of the *atan* function along X axis and Y_{adv} is the offset of the *atan* function along the Y axis for advancing values of contact angle.

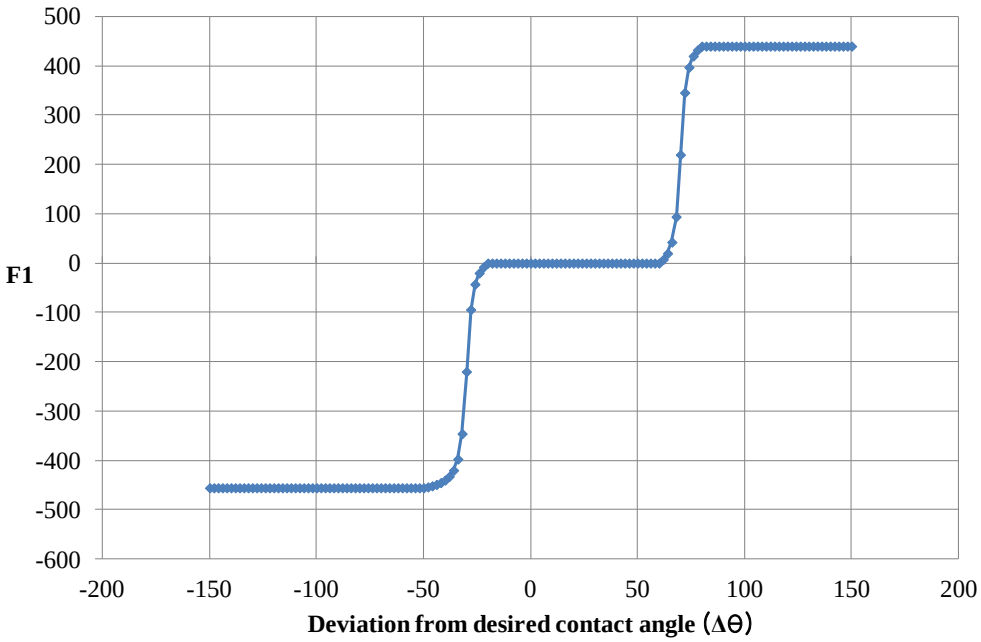

Fig. 38 Force dependence on contact angle deviation.

The plot of F_1 is asymmetric as it allows for individual tolerances for advancing and receding contact angles. $\Delta\theta$ is the deviation of contact angle from the desired range of contact angle. Fig. 38 shows the force dependence on contact angle graphically.

Fig. 39 shows the spatial dependence of the force on the scalar field in the direction along the wall and Fig. 40 shows the dependence on the perpendicular distance to the wall. Equations (18) and (19) show the dependence on the scalar field and on the normal distance from the wall.

$$F_2 = \cos\left(\frac{\phi}{T} * \frac{\pi}{2}\right) * \rho \tag{18}$$

$$F_3 = (H - d_{wall})^2 \tag{19}$$

where, H is the height and T is the thickness of the FAR. In this study T was used as 0.3184 mm and H was 0.398 mm. These values were found with a trial and error method and they may be correlated with the bubble size.

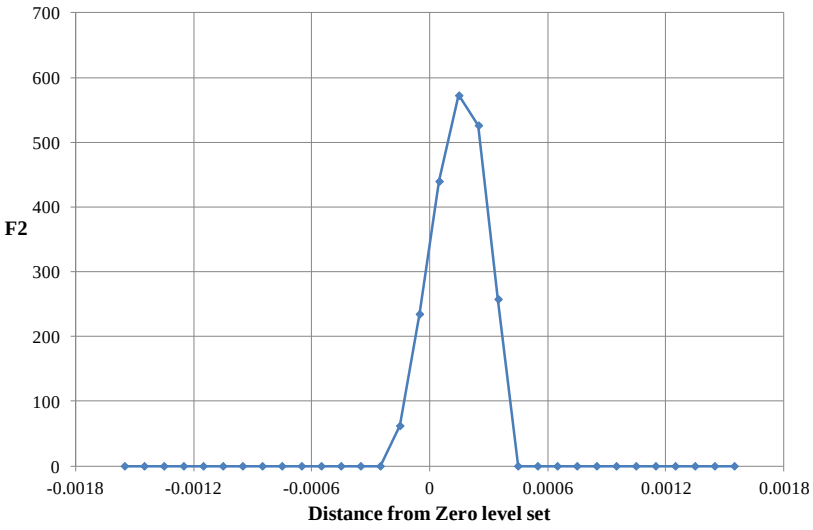

Fig. 39 Spatial dependence on distance field.

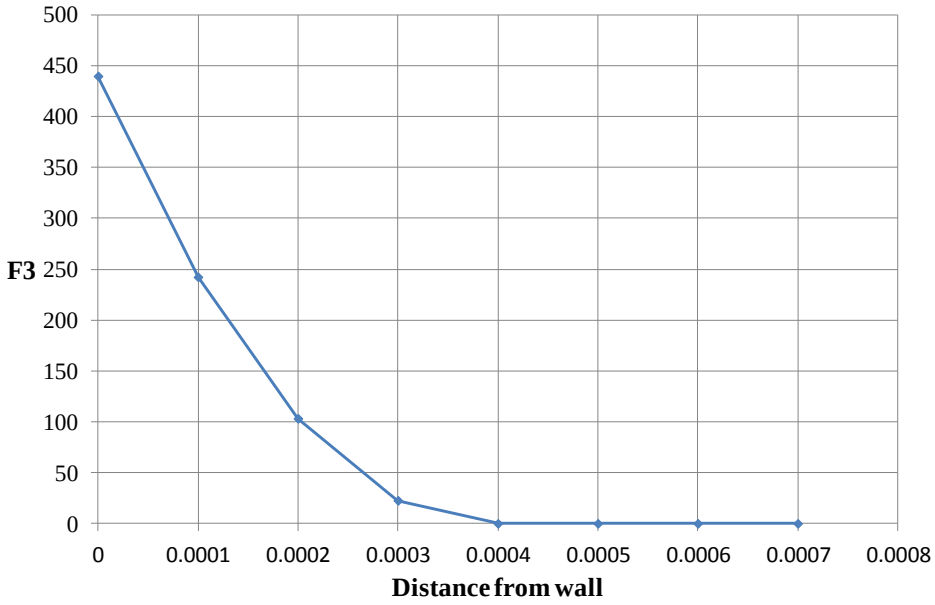

Fig. 40 Spatial dependence on distance from wall

Net contact force is the product of all three force components, i.e. $F_1F_2F_3$. Note ρ is a function of the scalar. This force was applied to the bubble and the average contact angle and force was monitored in the FAR. It is assumed that the force formulation which allows the achievement of the desired contact angle should be a close approximation of the contact force that acts on the bubble.

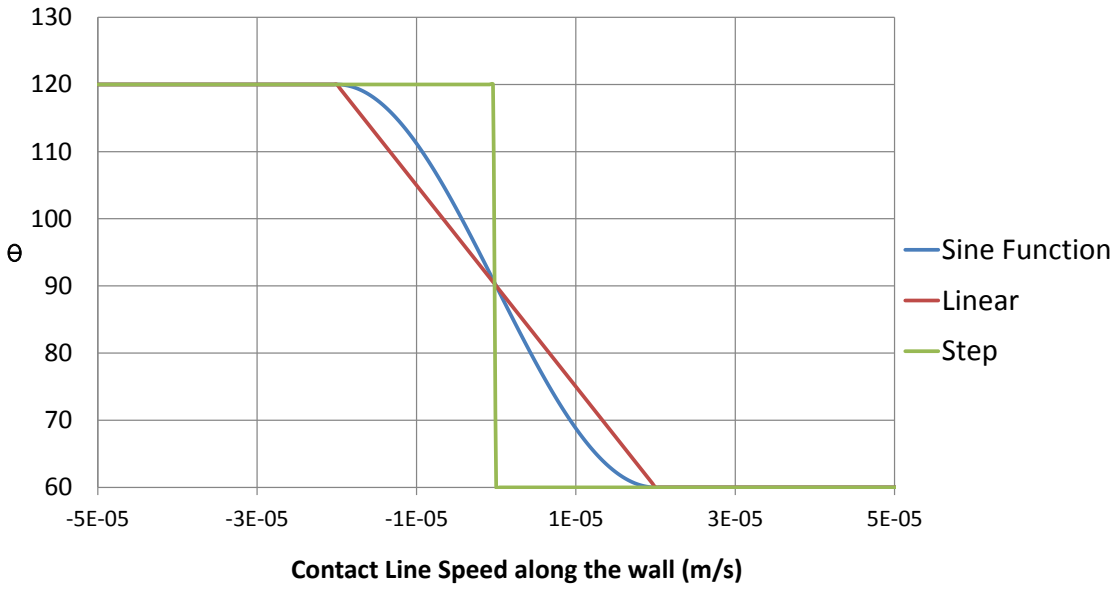

Fig. 41 Contact angle-contact line speed model

The desired dynamic contact angle along any point was determined by the model shown in Fig. 41. All the three interpolation models shown were tested for dynamic contact angle.

4.2 Influence of control algorithm on bubble wall interaction

The development of the control force algorithm is necessary for realistic modeling of sliding bubbles on walls. This force was applied to a single bubble and different parameters were varied to capture the effect of the force. Initially testing was done on static bubble cases without any buoyancy for studying the effect of force for static contact angles.

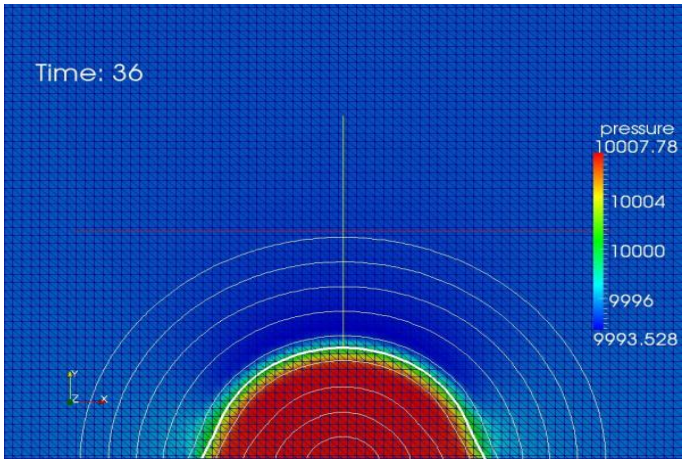

Fig. 42 Static contact angle of 110^o

Fig. 42 shows the snapshot of the evolution of a static bubble in contact with the wall with a prescribed contact angle of 110^o. This was also performed for acute contact angle of 60^o and is shown in Fig. 43. In the study of static contact angle no speed-angle model was implemented and the contact angle was the same at every point on the contact line. It was observed that the obtuse contact angle could be readily achieved however the acute contact angle was not achieved with desired accuracy.

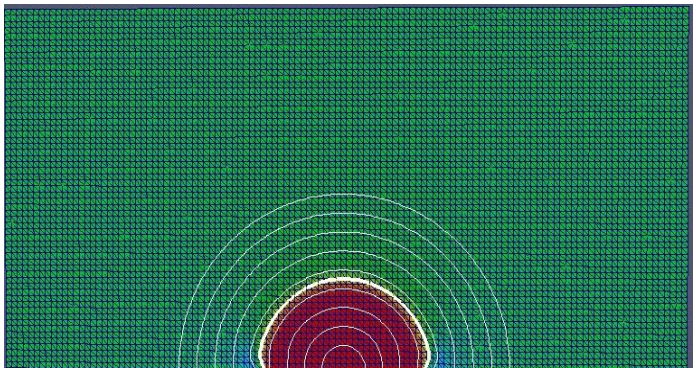

Fig. 43 Static contact angle of 60^o

This may be attributed to the fact that during application of contact force inwards a sharp kink in the interface tends to form and increase the local surface tension. This in turn makes the interface recover to smoothen the interface and thus it stops at a higher contact angle value than desired. Fig. 44 shows the evolution of the average static contact angle with respect to the time- step. Mesh independence study was carried out for static contact angle cases and the dashed line shows fine mesh simulation for 110^{o} and the dash-dot line shows coarse mesh simulation for 60^{o} contact angle.

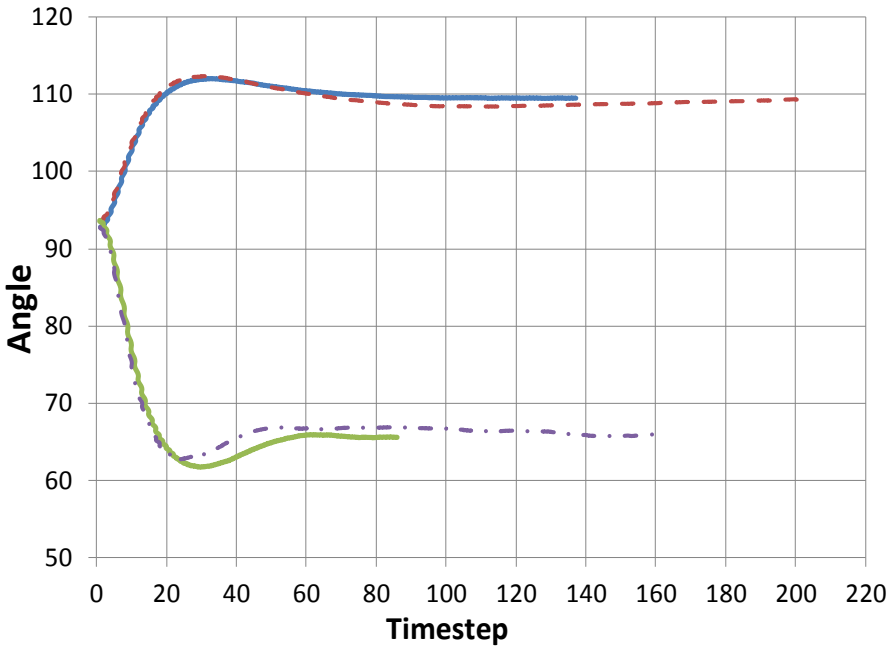

Fig. 44 Evolution of static contact angle

After establishing the application of static contact angle dynamic contact angle was implemented by applying different speed varying models. To study the effect of speed-contact angles three different models were proposed to relate contact line speed and contact

angle. It was found that for a bubble sliding on the wall it attained a terminal velocity (v_{term}) and v_{term} was not dependent on the type of interpolation applied. The shape and the wall dynamics were not affected by changing the interpolation model. After establishing the independence of this model this all the studies were done using a linear interpolation model in order to preserve continuity to maintain simplicity and rule out possible initiation of instabilities due to discontinuities.

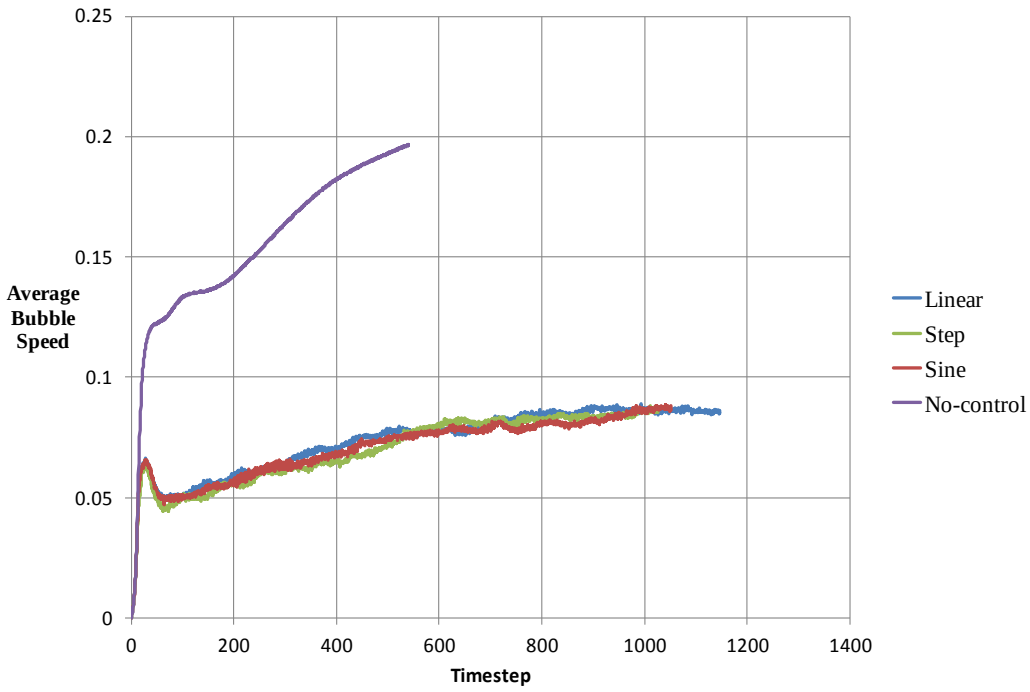

Fig. 45 Evolution of bubble velocity in no-control model and different interpolation models

Fig. 45 graphically depicts the temporal evolution of the average bubble velocity for no control force applied for advancing contact angle of 40^o, receding angle of 130^o and for

the three types of interpolation models. Fig. 46 shows the shape of the bubble for different interpolations at time step 400 (with a constant time step of 10^{-4} units). It may be concluded that the choice of interpolation model is not important and one might be able to use the step function to minimize computational effort.

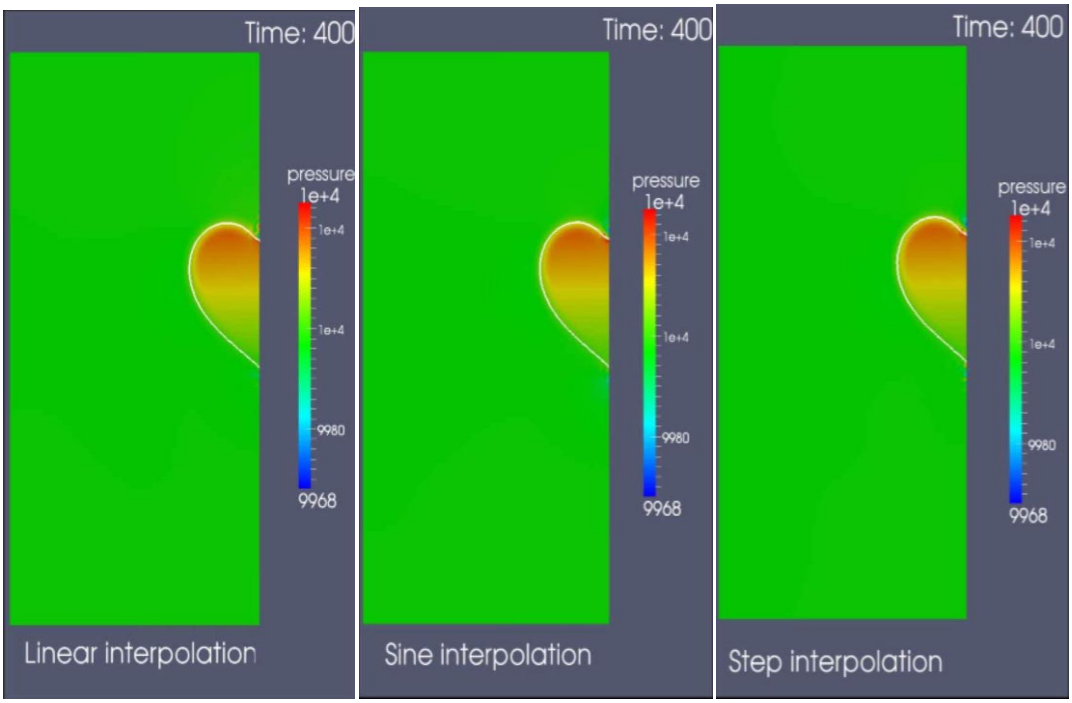

Fig. 46 Comparison of contact angle-speed models

To quantify the angular accuracy that may be achieved by the present control force algorithm the maximum and minimum angles were recorded with respect to time. It is assumed that the maximum and minimum contact angle should be close to the receding and advancing contact angle respectively. It was found that an accuracy range of about -5^{o} and

$+20^{o}$ was achieved for advancing and receding angles. This is shown in Fig. 47 which depicts evolution of maximum and minimum contact angles in the force application region.

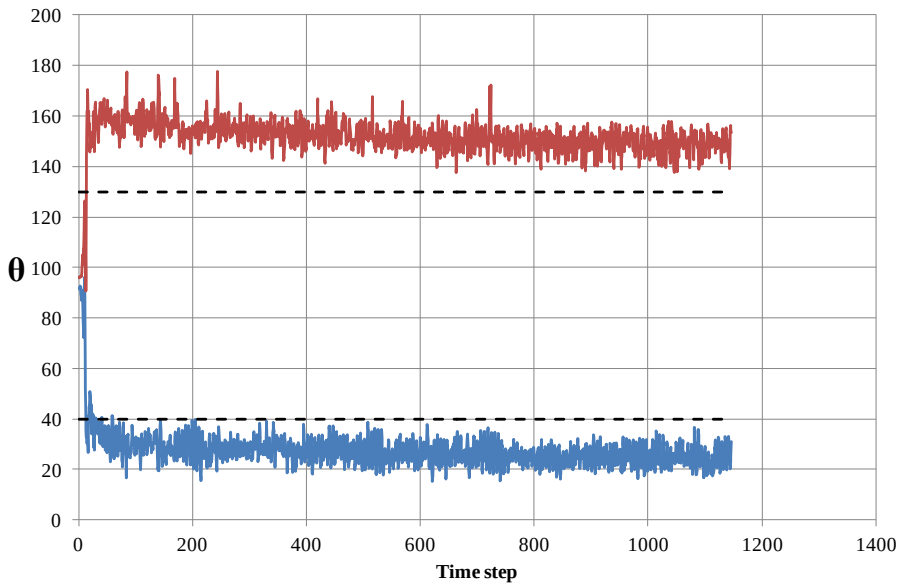

Fig. 47. Variation of advancing and receding contact angle over time (Target values shown as dashed lines)

5. CONCLUSION

A separate effect study was conducted to investigate the effect of nucleating bubbles on turbulent flow. Effective friction factor was estimated to develop boundary conditions for multiphase CFD applications. A rectangular half channel with periodic boundary conditions in the stream-wise and span-wise direction was meshed with a hexahedral grid and flow was simulated for $Re_\tau = 400$. Nucleating bubbles were approximated as rigid stationary hemispherical roughness elements at the wall and law of the wall constants and friction factor were calculated to characterize the effects of these roughness elements. It was found that different roughness densities affect the flow differently. As the density of roughness elements was varied a maximum friction factor of 0.038 was observed for roughness density of 151 roughness elements per cm^2. Uncertainty in the calculated friction factors was calculated for each case and the uncertainty was observed to be ranging from 0.83% to 5.7%. The uncertainty can be further reduced by accumulating more statistical data for these simulations. The effect of roughness density on law of the wall constants was also quantified. The law of the wall constant "B" flattens at the value of 1.0 at high roughness densities. It was observed that the turbulent kinetic energy peak shifts away from the wall as the roughness density increases. This was attributed to the suppression of turbulent flow structures occurring due to close spacing of the roughness elements. It was also observed that farther away from the wall the velocity profiles for different cases showed a tendency to merge together. Further the friction factor was found as a function of bubble density and was further correlated with wall superheat using the relation given by Dhir et. al. [10] for nucleation site density for subcooled flow boiling. The accuracy of this function was

calculated to be within $\pm$43.3%. The large error comes from the experimental uncertainty and is considered to be typical of experiments concerning heat and mass transfer. This particular result will help in estimating wall shear boundary conditions in low Weber number flows with nucleate boiling in heated channels. Relatively good uncertainty results from DNS simulation because of more available statistics. It may be remarked that this indicates the promise of DNS in the future. A large amount of data can be assimilated and processed through DNS in a cost effective manner which will lead to finer understanding of flow phenomenon such as that presented in this study.

Finally, a contact angle control algorithm was implemented in PHASTA to model the bubble-wall interaction. This force application is local and may be applied for multiple bubbles on the wall with a prescribed advancing and receding or static contact angles. The algorithm was tested on a single bubble sliding on the wall. It was shown that the interpolation used for relating the contact angle speed to the target local contact angle does not have a significant impact on the terminal bubble velocity.

6. FUTURE WORK

This study focused on channel flow simulations in order to develop fundamental ideas of influence of nucleating bubbles on turbulent flow.

Simulation of boiling in turbulent flows remains a challenge to the engineering community. Knowledge of effect of nucleating bubbles on the flow gives insight into the physics of subcooled nucleate boiling. Simulation of this regime is required to proceed towards simulation of flow boiling. Appendix I demonstrates implementation of the level set method in PHASTA to develop a bubbly flow simulation for a reactor subchannel. Combining the separate effect studies of bubbly flows and nucleating bubble flows we will develop better understanding of boiling flows. This study thus should be used as a stepping stone towards this goal.

The friction factor and the law of the wall developed here may also be implemented in flows with nucleating bubbles to have more efficient multiphase CFD simulations. The important limitation of this study has been the modeling of the bubbles as rigid elements. Contact force algorithm that was developed in this study may be used to simulate bubble behavior at the wall more accurately. This was done to expand the current study by using level set modeling in PHASTA for a bubble sitting at the wall. However it remains to be investigated as to how such algorithms function on large meshes such as the ones used in this study (~40M) and how do they handle bubble coalescence which is bound to occur while simulating higher densities of multiple deformable nucleating bubbles. This study should also quantify the variation of results due to difference in modeling of bubbles. The future studies in this particular area will be invaluable in understanding boiling in turbulent flows and will

benefit the fundamentals of fluid dynamics, multiphase CFD, two-fluid models and heat transfer applications.

BIBLIOGRAPHY

[1] R. Lahey, "The simulation of multidimensional multiphase flows," *Nuclear Engineering and Design,* vol. 235, p. 1043–1060, 2005.

[2] I. Bolotnov, K. Jansen, D. Drew, A. Oberai and R. T. Lahey, Jr., "Detached Direct Numerical Simulation of Turbulent Two-phase Bubbly Channel Flow," *Int. J. Multiphase Flow,* vol. 37, pp. 647-659, 2011.

[3] I. A. Bolotnov, "Influence of Bubbles on Turbulence Anistropy," *Journal of Fluids Engineering,* vol. 135(5), pp. 051301-051301-9, 2013.

[4] D. Chatzikyriakou, J. Buongiorno and D. Lakehal, "Benchmarks for Interface-Tracking Codes in the Consortium for Advanced Simulation of LWRs (CASL)," in *4th International Topical Meeting on Nuclear Reactor Thermal Hydraulics (NURETH-14),* Toronto, Ontario, Canada, September 25-29, 2011.

[5] R. Moser, J. Kim and N. Mansour, "Direct numerical simulation of turbulent channel flow up to Ret = 590," *Phys. Fluids,* vol. 11, pp. 943-945, 1999.

[6] A. V. Trofimova, A. E. Tejada-Martínez, K. E. Jansen and R. T. Lahey, Jr., "Direct numerical simulation of turbulent channel flows using a stabilized finite element method," *Computers & Fluids,* vol. 38, pp. 924-938, 2009.

[7] P. A. Krogstad, H. I. Andersson, O. M. Bakken and A. Ashrafian, "An experimental and numerical study of channel flow with rough walls," *J. Fluid Mech.,* vol. 530, pp. 327-352, 2005.

[8] A. Ashrafian, H. I. Andersson and M. Manhart, "DNS of turbulent flow in a rod-roughened channel," *Heat and Fluid Flow,* vol. 25, pp. 373-383, 2004.

[9] L. Z. Zeng and J. F. Klausner, "Nucleation Site Density in Forced Convection Boiling," *Journal of Heat Transfer,* vol. 115, pp. 215-221, 1993.

[10] N. Basu, G. Warrier and V. K. Dhir, "Onsent of Nucleate Boiling and Active Nucleation Site Density During Subcooled Flow Boiling," *Journal of Heat Transfer,* vol. 124, pp. 717-728, 2002.

[11] E. Aktinol and V. Dhir, "Numerical Simulation of Nucleate Boiling Phenomenon Coupled with Thermal Response of the Solid," *Microgravity Science and Technology,* vol. 24, no. 4, pp. 255-265, 2012.

[12] M. Renardy, Y. Renardy and J. Li, "Numerical Simulation of Moving Contact Line Problems Using a Volume-of-Fluid Method," *Journal of Computational Physics,* vol. 171, no. 1, p. 243–263, 2001.

[13] H. Liu, S. Krishnan, S. Marells and H. S. Udaykumar, "Sharp interface Cartesian grid method II: A technique," *Journal of Computational Physics,* vol. 210, no. 1, pp. 32-54, 2005.

[14] S. Afkhami and M. Bussmann, "Drop Impact Simulation with a Velocity-Dependent Contact Angle," in *ILASS Americas 19th Annual Conference on Liquid Atomization and Spray Systems,* Tornto, May 2006.

[15] K. E. Jansen, "A stabilized finite element method for computing turbulence," *Comp. Meth. Appl. Mech. Eng.,* vol. 174, pp. 299-317, 1999.

[16] C. H. Whiting and K. E. Jansen, "A stabilized finite element formulation for the incompressible Navier-Stokes equations using a hierarchical basis," *International Journal of Numerical Methods in Fluids,* vol. 35, pp. 93-116, 2001.

[17] K. E. Jansen, "Unstructured grid large eddy simulations of wall bounded flows," *Annual Research Briefs, Center for Turbulence Research, NASA Ames/Stanford University,* p. 151, 1993.

[18] O. Sahni, J. Mueller, K. E. Jansen, M. S. Shephard and C. A. Taylor, "Efficient anisotropic adaptive discretization of the cardiovascular system," *Computer Methods in Applied Mechanics and Engineering,* vol. 195, no. 41-43, pp. 5634-5655, 2006.

[19] A. E. Tejada-Martinez and K. E. Jansen, "A parametric-free dynamic subgrid-scale model for large-eddy simulation," *Computer Methods in Applied Mechanics and Engineering,* vol. 194, no. 9, pp. 1225-1248, 2005.

[20] S. Nagrath, K. E. Jansen, R. T. Lahey and I. Akhatov, "Hydrodynamic simulation of air bubble implosion using a FEM based level set approach," *Journal of Computational Physics,* vol. 215, pp. 98-132, 2006.

[21] M. Zhou, O. Sahni, H. Jin Kim, C. A. Figueroa, C. A. Taylor, M. S. Shephard and K. E. Jansen, "Cardiovascular flow simulation at extreme scale," *Comput. Mech.,* vol. 46, pp. 71-82, 2010.

[22] C. Colebrook, "Turbulent flow in pipes, with particular reference to the transition region between smooth and rough pipe laws," *Journal of Institution of Civil Engineers (London),* vol. 11, pp. 133-156, 1939.

[23] O. M. Bakken and P. A. Krogstad, "Stress measurements in a rough wall channel flow using a variable angle method of calibration for X-probes," in *Proceedings of the Third International Symposium on Turbulence and Shear Flow Phenomena*, 2003.

APPENDIX

Appendix I : Law of the wall for smooth subchannel

A subchannel simulation for Re_τ= 400 was developed and run locally. However the mesh had to be kept coarse at 0.8 million nodes instead of the required 9 million nodes because of the limited local memory resources. This simulation was run on just 64 cores (compared to the cases studied in the main text that were run on 6000-10000 cores). Thus, as such this simulation does not resolve the turbulence entirely. A smooth subchannel simulation was developed with periodic boundary conditions in the stream-wise (x) and both transverse (y, z) directions. All the curved surfaces were designated as walls with no slip boundary conditions. The boundary layer was resolved with 13 layers varying in thickness from estimated 1 wall units (w.u., equivalent to size of one y+) at the wall to 10 w.u. in the bulk with a growth factor of 1.2. The mesh for the subchannel is shown in Fig. 48.

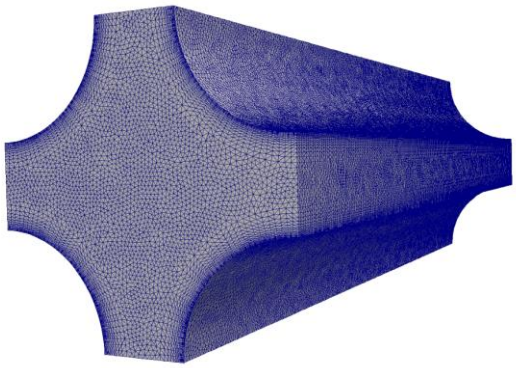

Fig. 48 Mesh for subchannel simulation.

The table detailing the mesh for boundary layer growth (for 13 layers) and bulk mesh is given in Appendix II.

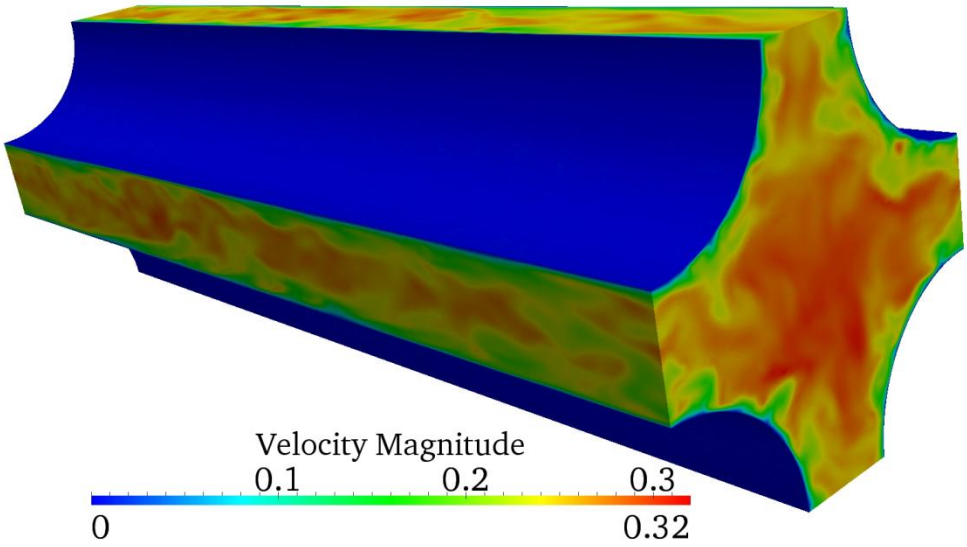

Fig. 49 Subchannel flow field

Fig. 49 shows the flow field within the subchannel. To gather statistical data a number of probes were deployed within the subchannel near the inlet plane. The plane containing the probes for measuring the flow was kept perpendicular to the flow direction. The Probe locations are shown in Fig. 50.

The probes are placed in such a way that for a constant radial distance the azimuth of probes varies. In this way we may get an averaged velocity at a particular distance from the

wall. When this averaging is done for each distance from the wall to the centerline we may get the law of the wall.

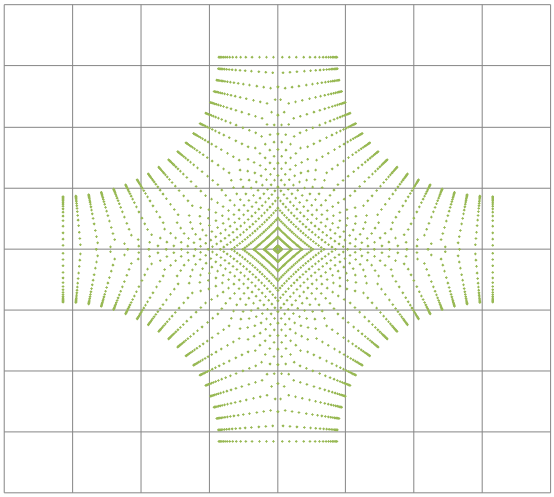

Fig. 50 Probe locations for subchannel

Using the capabilities of PHASTA it is possible to introduce vapor phase into the developed single phase turbulence. The study of the influence of bubbles on the flow within a subchannel holds considerable interest for the nuclear engineering community. To introduce the bubbles (1% void fraction) the mesh size has to be increased considerably to properly resolve the bubbles (with at least 20 nodes across). Mesh refinement was done for the coarse subchannel case presented earlier and the single phase solution was transferred to this new refined mesh using PHASTA tools. Fig. 51 shows the bubbles that have been introduced in the domain with the developed single phase turbulence.

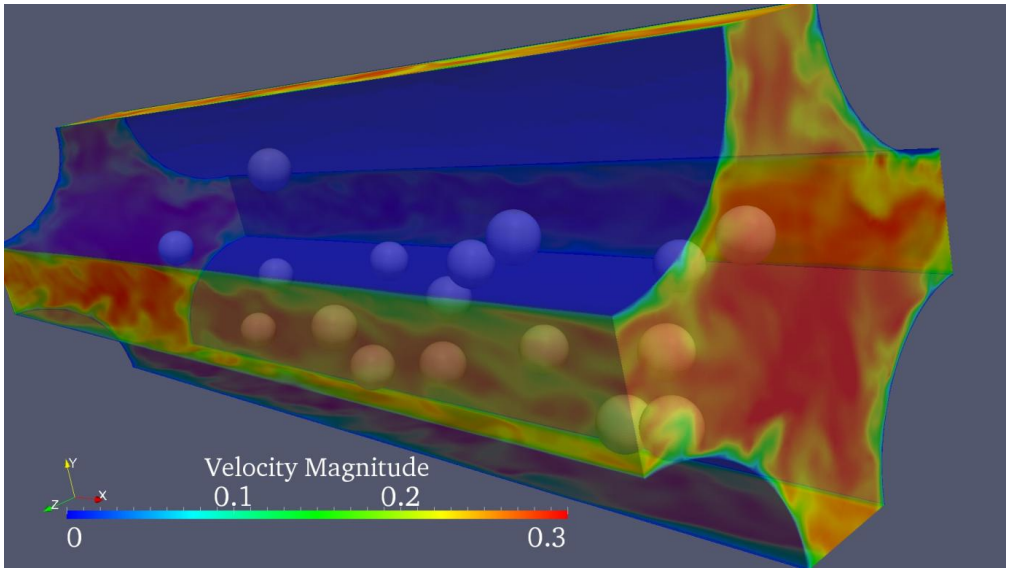

Fig. 51 Two-phase bubbly flow simulation snapshot for subchannel in developed turbulent flow field

Appendix II : Mesh for the subchannel

Table 9 Mesh node height from the wall for subchannel case

Boundary layer number	Cell resolution, (in meter)	Node Distance from wall(m)	Resolution,(in non dimensional wall units	Distance from the wall (in wall units)
1	2.46E-05	0.00E+00	2.54E+00	0.00E+00
2	2.95E-05	2.46E-05	3.05E+00	2.54E+00
3	3.54E-05	5.40E-05	3.66E+00	5.59E+00
4	4.24E-05	8.94E-05	4.39E+00	9.25E+00
5	5.09E-05	1.32E-04	5.27E+00	1.36E+01
6	6.11E-05	1.83E-04	6.33E+00	1.89E+01
7	7.33E-05	2.44E-04	7.59E+00	2.52E+01
8	8.80E-05	3.17E-04	9.11E+00	3.28E+01
9	1.06E-05	4.05E-04	1.09E+00	4.19E+01
10	1.27E-04	5.11E-04	1.31E+01	5.29E+01
11	1.52E-04	6.37E-04	1.57E+01	6.60E+01
12	1.82E-04	7.90E-04	18.9E+01	8.17E+01
13	2.19E-04	9.72E-04	2.27E+01	1.01E+02
14	2.05E-04	1.19E-03	2.12E+01	1.23E+02
15	2.05E-04	1.40E-03	2.12E+01	1.44E+02
16	2.05E-04	1.60E-03	2.12E+01	1.66E+02
17	2.05E-04	1.80E-03	2.12E+01	1.87E+02
18	2.05E-04	2.01E-03	2.12E+01	2.08E+02
19	2.05E-04	2.21E-03	2.12E+01	2.29E+02
20	2.05E-04	2.42E-03	2.12E+01	2.50E+02
21	2.05E-04	2.62E-03	2.12E+01	2.72E+02
22	2.05E-04	2.83E-03	2.12E+01	2.93E+02
23	2.05E-04	3.03E-03	2.12E+01	3.14E+02
24	2.05E-04	3.24E-03	2.12E+01	3.35E+02
25	2.05E-04	3.44E-03	2.12E+01	3.56E+02
26	2.05E-04	3.65E-03	2.12E+01	3.78E+02
27	2.05E-04	3.85E-03	2.12E+01	3.99E+02

28	2.05E-04	4.06E-03	2.12E+01	4.20E+02
29	2.05E-04	4.26E-03	2.12E+01	4.41E+02